



ESA Climate Change Initiative (CCI+) Essential Climate Variable (ECV) Greenland_Ice_Sheet_cci+ (GIS_cci+)

Algorithm Theoretical Basis Document (ATBD)

Prime & Science Lead: Louise Sandberg Sørensen
DTU Space, Copenhagen, Denmark

Technical Officer: Anna Maria Trofaier
ESA ECSAT, Didcot, United Kingdom

Consortium:

- Asiaq Greenland Survey (ASIAQ)
- DTU-Space, Department of Geodynamics (DTU-S)
- DTU-Space, Department of Microwaves and Remote Sensing (DTU-N)
- Danish Meteorological Institute (DMI)
- ENVironmental Earth Observation IT GmbH (ENVEO)
- Science [&] Technology AS (S&T)
- Technische Universität Dresden (TUDr)
- The Geological Survey of Denmark and Greenland (GEUS)
- The Niels Bohr Institute (NBI)
- Northumbria University (NU)
- University of Leeds (UL)



Signatures page

Prepared by	Jan Wuite Lead Author, ENVEO		Date: 1 December 2023
Issued by	Daniele Fantin, Project Manager, S[&]T		Date: 1 December 2023
Checked by	Louise Sørensen Science Leader, DTU-S		Date: 1 December 2023
Approved by	Anna Maria Trofaier ESA Technical Officer		Date: 1 December 2023

Table of Contents

Change Log.....	6
Acronyms and Abbreviations.....	7
1 Introduction.....	9
1.3 Applicable and Reference Documents.....	9
2 Surface Elevation Change.....	11
2.1 Introduction.....	11
2.2 Review of scientific background.....	11
2.3 Algorithms.....	11
2.4 Input data and algorithm output.....	13
2.4.1 Input data.....	14
2.4.2 Algorithm Update.....	14
2.5 Accuracy and performance.....	15
2.6 Capabilities and known limitations.....	15
2.7 References.....	16
3 Ice Velocity (SAR).....	17
3.1 Introduction.....	17
3.2 Review of scientific background.....	17
3.3 Algorithms.....	19
3.3.1 SAR Offset Tracking.....	19
3.3.2 SAR Interferometry.....	20
3.3.3 Combined InSAR and OT.....	23
3.3.4 Remarks.....	24
3.4 Input data and algorithm output.....	24
3.4.1 Input Data.....	24
3.4.2 Algorithm output.....	25
3.5 Accuracy and performance.....	25
3.6 Capabilities and known limitations.....	26
3.7 InSAR Line-of-sight velocity prototype product.....	27
3.8 References.....	27
4 Ice Velocity (Optical).....	29
4.1 Introduction.....	29
4.2 Review of scientific background.....	29
4.3 Algorithm.....	29
4.3.1 The Optical IV feature tracking algorithm.....	30
4.3.2 Processing pipeline.....	30
4.4 Input data and algorithm output.....	32
4.4.1 Input data.....	32



4.4.2 Algorithm output.....	32
4.5 Accuracy and performance.....	32
4.6 Capabilities and known limitations.....	33
4.7 References.....	33
5 Gravimetric Mass Balance.....	34
5.1 Introduction.....	34
5.2 Scientific background update.....	34
5.3 Algorithms.....	36
5.4 Input data and algorithm output.....	37
5.5 Capabilities and known limitations.....	37
5.6 References.....	37
6 Mass Flow Rate and Ice Discharge.....	39
6.1 Introduction.....	39
6.2 Review of scientific background.....	39
6.3 Algorithms.....	40
6.3.1 Terminology.....	40
6.3.2 Gate Location.....	40
6.3.3 Thickness.....	41
6.3.4 Missing or invalid data.....	41
6.3.5 Discharge.....	41
6.4 Input data and algorithm output.....	42
6.4.1 Input Data.....	42
6.4.2 Algorithm Output.....	42
6.5 Accuracy and performance.....	42
6.5.1 Accuracy.....	42
6.5.2 Performance.....	44
6.6 Capabilities and known limitations.....	45
6.7 References.....	45
7 Supraglacial Lakes (SGL).....	48
7.1 Introduction.....	48
7.2 Review of scientific background.....	48
7.3 Algorithms.....	48
7.4 Input data and algorithm output.....	51
7.5 Performance Measures.....	51
7.6 Capabilities and known limitations.....	51
7.7 References.....	51
8 Calving Front Locations.....	53
8.1 Introduction.....	53
8.2 Review of scientific background.....	53
8.3 Algorithms.....	54



8.4 Input data and algorithm output.....	55
8.5 Processing.....	55
8.6 Capabilities and limitations.....	55
8.7 References.....	56



Change Log

Issue	Author	Affected Section	Change	Status
0.6	ENVEO	All	Draft version	
1.0	All	All	First version	
1.1	GEUS	6	Update on MFID	
1.2	ASIAQ	7	Update on SGL	
1.3	DTU	All	Update on SEC and edits	
1.4	S&T	4, 8	Update on Opt IV and inclusion of CFL	Released to ESA
2.0	ENVEO	All	Update for Phase 2	Released to ESA



Acronyms and Abbreviations

Acronyms	Explanation
ATBD	Algorithm Theoretical Basis Document
C3S	Copernicus Climate Change Service
CCI	Climate Change Initiative
CFL	Calving Front Location
CONAE	Comisión Nacional de Actividades Espaciales
CS2	CryoSat-2
CSR	Center for Space Research, University of Austin
DEM	Digital Elevation Model
(D)InSAR	(Differential) Interferometric Synthetic Aperture Radar
DL	Deep Learning
DMI	Danish Meteorological Institute
DTU-N	DTU Microwaves and Remote Sensing Group
DTU-S	DTU Geodynamics Group
E3UB	End-to-End ECV Uncertainty Budget
ECV	Essential Climate Variable
ENU	East North Up
ENVEO	ENVironmental Earth Observation IT GmbH
EO	Earth Observation
ESA	European Space Agency
GCOS	Global Climate Observation System
GCP	Ground Control Point
GEUS	Geological Survey of Denmark and Greenland
GFZ	Deutsche GeoForschungsZentrum
GIA	Glacial Isostatic Adjustment
GIS	Greenland Ice Sheet
GLL	Grounding Line Location
GMB	Gravimetry Mass Balance
GRACE(FO)FO)	Gravity Recovery and Climate Experiment (Follow On)
IMBIE	Ice Sheet Mass Balance Inter-Comparison Exercise
InSAR	Interferometric Synthetic Aperture Radar
IPP	Interferometric Post-Processing
IV	Ice Velocity
JPL	NASA Jet Propulsion Laboratory



MAI	Multiple Aperture Interferometry
MFID	Mass Flux and Ice Discharge
NBI	Niels Bohr Institute, University of Copenhagen
NEGIS	North East Greenland Ice Stream
NU	Northumbria University
OT	Offset Tracking
PROMICE	Danish Program for Monitoring of the GIS
RA	Radar Altimetry
RMS	Root Mean Square
S&T	Science and Technology AS
S2	Sentinel-2
SAR	Synthetic Aperture Radar
SEC	Surface Elevation Change
SLR	Satellite Laser Ranging
SMB	Surface Mass Balance
SOW	Statement of Work
TEC	Total Electron Content
TOA	Top of Atmosphere
TPROP	Technical Proposal
TUDr	Technische Universität Dresden
UL	University of Leeds
URD	User Requirement Document
TOPS	Terrain Observation by Progressive Scans

1 Introduction

1.1 Purpose and Scope

This document contains the Algorithm Theoretical Basis for the Greenland_Ice_Sheet_cci (GIS_cci) project for CCI+ Phase 2, in accordance with contract and SoW (AD1, AD2 and AD3). The ATBD describes the scientific background and principle of the algorithms, their expected or known accuracy and performance, input, and output data, as well as capabilities and limitations.

The ATBD for the Ice Sheets cci project (RD1) is used as a basis for this work. It describes the algorithms used to generate the ECV parameters 'Surface Elevation Change (SEC)', 'Ice Velocity (IV)', 'Calving Front Location (CFL)', 'Grounding Line Location (GLL)' and 'Gravimetric Mass Balance (GMB)'. The current document is a supplement to this, and the aim is to review and provide an update regarding improvements to existing algorithms, proposed for CCI+, and to document the theoretical basis for new algorithms implemented for Mass Flux and Ice Discharge (MFID) and SupraGlacial Lakes (SGL)

1.2 Document Structure

This document is structured into an introductory chapter followed by 6 chapters focussed on the retrieval algorithms for each of the CCI+ parameters:

- Surface Elevation Change (SEC)
- Ice Velocity (IV-SAR)
- Ice Velocity (IV-Optical)
- Gravimetric Mass Balance (GMB)
- Mass Flow Rate and Ice Discharge (MFID)
- Supraglacial Lake (SGL)
- Calving Front Location (CFL) - Out of production

1.3 Applicable and Reference Documents

Table 1.1: List of Applicable Documents

No	Doc. Id	Doc. Title	Date	Issue/ Revision/ Version
AD1	ESA/Contract No. 4000126523/19/I-NB - Greenland_Ice-Sheets_CCI+ and its Appendix 1 (incl CCN3)	CCI+ Phase 1 New R&D pm CCI ECVs for Greenland_Ice Sheet_cci (incl CCN3)	Cont: 2019.03.06 CCN3: 2022.12.05	-
AD2	ESA-EOP-SC-AMT-2021-53	Climate Change Initiative Extension (CCI+) Phase 2 - New R&D on CCI Essential Climate Variables -SoW (incl Annexes)	2022.06.10	Issue 1 Revision 2



Table 1.2: List of Reference Documents

No	Doc. Id	Doc. Title	Date	Issue/ Revision/ Version
RD1	ST-DTU-ESA-GISCCI-ATBD-001-v3.2	Greenland_Ice_Sheet_cci Algorithm Theoretical Baseline Document (ATBD)	2017.11.24	3.2
RD2	ST-DTU-ESA-GISCCI+-ATBD-001	Greenland_Ice_Sheet_cci+ Algorithm Theoretical Baseline Document (ATBD)	2021.10.28	1.4

Note: If not provided, the reference applies to the latest released Issue/Revision/Version



2 Surface Elevation Change

2.1 Introduction

Satellite altimetry provides estimates of ice sheet elevation changes through repeated measurements of ice sheet surface elevations. The technique has been employed to study both Greenland (e.g., Sørensen et al., 2018; Slater et al. 2019; IMBIE Team 2019) and Antarctica (e.g., IMBIE Team 2018, Schröder et al., 2019), and has the distinct advantage of being able to resolve the detailed pattern of mass imbalance, with frequent (up to monthly) temporal sampling. Radar altimetry provides the longest continuous observational record of all geodetic techniques going back to 1991.

Altimeters using microwave frequencies are commonly referred to as radar altimetry. At these wavelengths, the signal can penetrate cloud cover, making the measurements possible in all weather conditions. In addition, the use of microwaves enables measurements to be made independently from sunlight conditions. The satellites with altimeters onboard are placed in repeat orbits (covering a region of up to 1 km on either side of a nominal ground track) enabling systematic monitoring of the Earth.

Currently, several satellite altimeters are monitoring the cryosphere; CryoSat-2 with its unique SARIn technique/mode to map the margins of the ice sheet, Sentinel-3 that has the capability to using SAR at the ice sheet margin, and ICESat-2 which is a photon-counting altimeter operated by NASA. Within GIS CCI+ we currently include only RA data in our SEC solutions, but future data releases will also include ICESat-2.

(RD2) provides a thorough explanation of the current GIS CCI processor. Here, we shift our focus to the next phase, transitioning from 5-year overlapping SEC data to time steps of Δt derived from gridded model parameters.

2.2 Review of scientific background

We refer to the review of the scientific background already presented in (RD1) and describe here the relevant literature that has been published since (RD1).

The GIS CCI SEC processor and products have been presented in Sørensen et al., (2018), and the results were also included in the Mottram et al., (2019) paper. One of the main challenges of using RA to map SEC is the fact that the RA might penetrate the snow and track subsurface layers. Simonsen & Sørensen, (2017) presented a thorough assessment of the best algorithms to be used for CryoSat-2 data to minimize the effect of changing penetration depth.

Slater, T. (2019b) has presented an alternative approach of separating surface and volume scattering in CryoSat-2 data which looks like a promising approach, although it requires analysis at RA waveform level, and within CCI+ we are currently making use of ESA L2 products only.

2.3 Algorithms

There are two algorithms implemented for SEC production in the GIS CCI+ project.

1. TR (true repeat track)
2. PF (Plane-fit)

These are already described in detail in (RD1) and in Sørensen et al., (2018) and will not be explained further here, but in Table 2.1 we indicate which algorithm is used for the creation of each 5-year SEC products. In previous versions also an AT (along track) algorithm was implemented, but in the current processor this has been replaced by the PF algorithm.



Table 2.1: Satellite data and algorithms used for each of the 5-yr SEC grids.

Period	Mission(s)	SEC algorithm
1992-1996	ERS-1 / ERS-2	TR
1993-1997	ERS-1 / ERS-2	TR
1994-1998	ERS-1 / ERS-2	TR
1995-1999	ERS-1 / ERS-2	TR
1996-2000	ERS-2	TR
1997-2001	ERS-2	TR
1998-2002	ERS-2	TR
1999-2003	ERS-2 / Envisat	TR
2000-2004	ERS-2 / Envisat	TR
2001-2005	ERS-2 / Envisat	TR
2002-2006	ERS-2 / Envisat	TR
2003-2007	ERS-2 / Envisat	TR
2004-2008	ERS-2 / Envisat	TR
2005-2009	Envisat	TR
2006-2010	Envisat	TR
2007-2011	CryoSat-2 / Envisat	PF
2008-2012	CryoSat-2 / Envisat	PF
2009-2013	CryoSat-2 / Envisat	PF
2010-2014	CryoSat-2 / Envisat	PF
2011-2015	CryoSat-2 / Envisat	PF
2012-2016	CryoSat-2 / Envisat	PF
2013-2017	CryoSat-2 / Sentinel-3	PF
2014-2018	CryoSat-2 / Sentinel-3	PF
2015-2019	CryoSat-2 / Sentinel-3	PF
2016-2020	CryoSat-2 / Sentinel-3	PF
2017-2021	CryoSat-2 / Sentinel-3	PF
2018-2022	CryoSat-2 / Sentinel-3	PF
2019-2023	CryoSat-2 / Sentinel-3	PF

2.4 Input data and algorithm output

Figure 2.1 shows the processing lines for TR and PF (exemplified by CryoSat-2 input-data), the two, algorithms used to derive SEC.

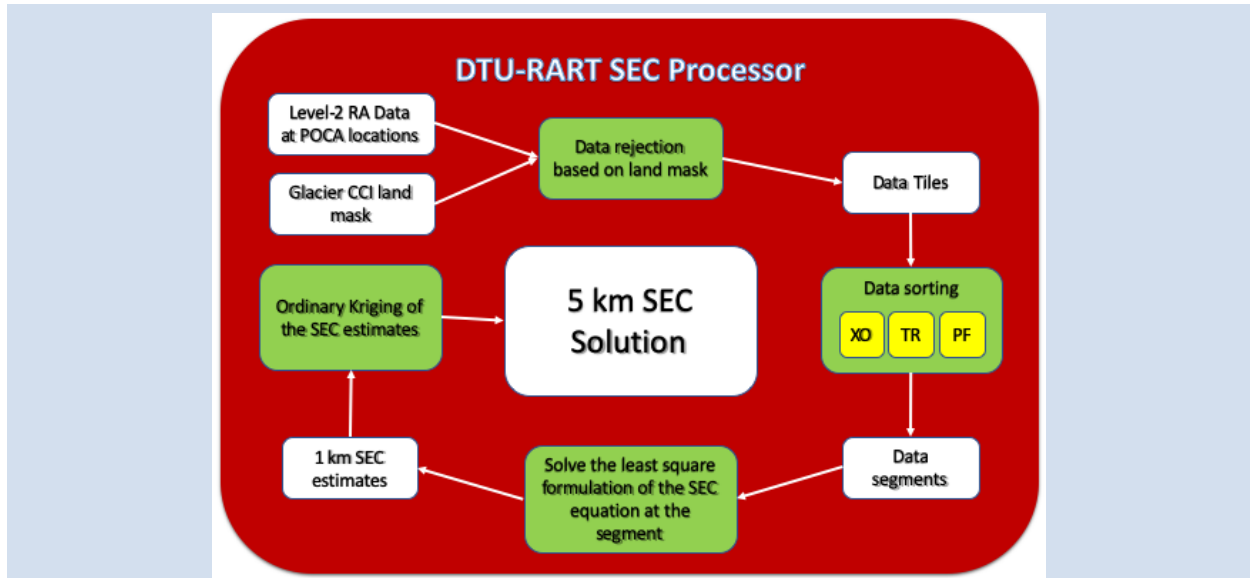


Figure 2.1: Workflow of the DTU-RART SEC processor.

The processing chain for TR and PF are described in (RD2) and will not be explained further here. Here, we describe the next evolution of the data from 5-year overlapping SEC data to timesteps of dh from gridded model parameters.

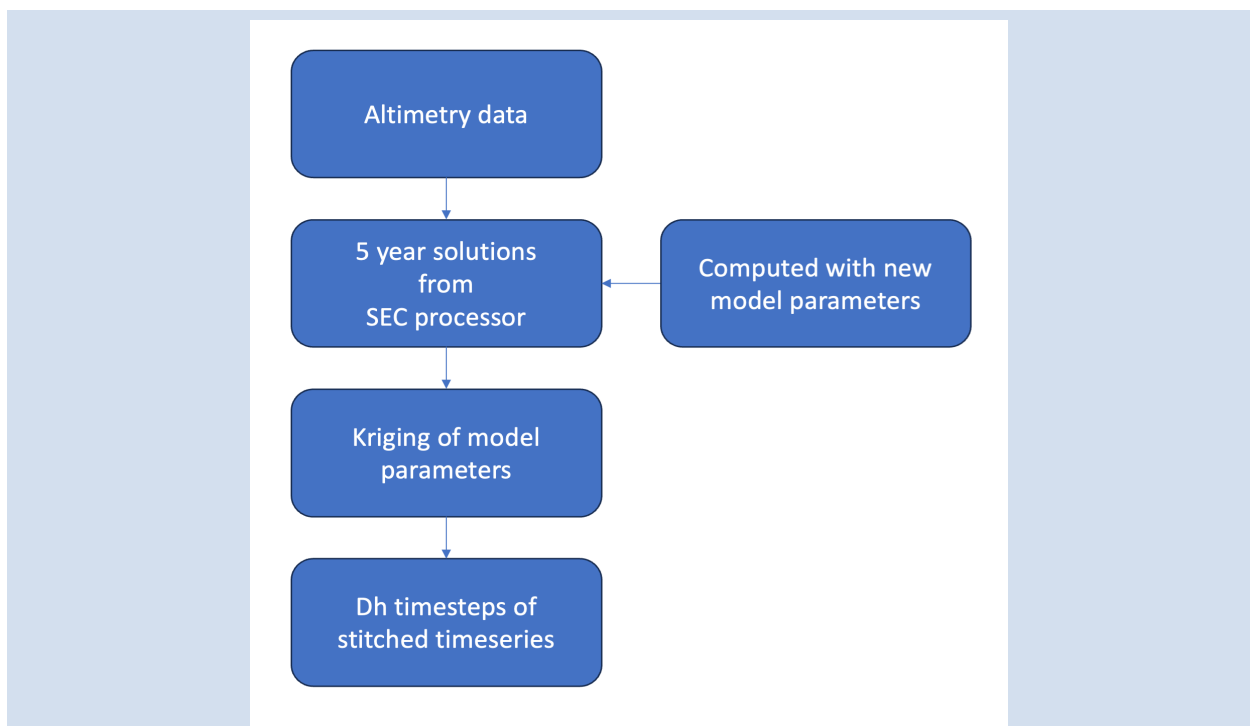


Figure 2.2: Updated workflow of the DTU-RART SEC processor

2.4.1 Input data

The main improvements of the SEC processor are changes in the computed model parameters and post processing of the parameters. These improvements are described below.

Ice mask

One of the improvements of the SEC processor within the CCI+ project is a change of one of the input datasets required. In the previous version as described in (RD1) the ice mask used in the processing line (See Figure 2-1), was generated from a digitized glacier outline that is now outdated. Therefore, we have changed the ice mask to be that of “gi_rgi05_003” (strongly connected glaciers + ice sheet) available through the Glacier CCI Database <http://glaciers-cci.enveo.at/crdp2/index.html>.

This data set is an update of gi_rgi05_001 and including only the peripheral glaciers and ice caps with connectivity level CL2 (strong connection to the ice sheet) and the updated ice sheet outline (Rastner et al., 2012).

This choice of using a new ice mask furthermore ensures consistency between CCI+ products as also the IV processor uses this ice mask.

RA data

The SEC processor utilizes more than 25 years of ESA radar altimetry observation, from six different satellites: ERS-1 and ERS-2, ENVISAT, CryoSat-2, and the two Sentinel-3 satellites A/B.

DEM

In the Greenland CCI SEC product, the GIMP-DEM was used as auxiliary DEM in the processing (RD1), for current CCI+ processing is the GIMP-DEM replaced by the newer ArcticDEM.

2.4.2 Algorithm Update

The model used to calculate the elevation changes has the following formula:

$$H(x, y, t) = H_0(x, y) + dHdt(t - \underline{t}) + dHdt(t - \underline{t})^2 + a \cdot \cos(\omega \cdot (t - \underline{t})) + b \cdot \sin(\omega \cdot (t - \underline{t}))$$

Depending on the satellite mission additional model parameters can be included, such as waveform parameters, ascending, descending and mission biases.

For the equation above (eq ref) dHdt represents the instantaneous change in height for time t. The factor (t - \underline{t}) represents the time elapsed since the reference time \underline{t} .

The last two terms including a and b describe the seasonal variations in the model. These variations are periodic changes in height that repeat with a specific frequency and amplitude, representing the seasonal changes in height. Including the dH/dt² term shows that the change in height cannot always be assumed to be linear over time.

These 5 model parameters are computed for each 5-year overlapping SEC data and are interpolated onto a common grid. For this, we use the geostatistical interpolation method known as kriging, which takes into account the spatial variation and coherence in the input dataset. This information is used to create a variogram, describing the geospatial relationships in the field. Subsequently, this variogram is employed in the interpolation process to weigh nearby observations to generate an optimally weighted average of these values.

We perform kriging on the anomaly fields of the model parameters, and finally, the average parameter field is added. This allows us to estimate the optimal values of the model parameters throughout our grid. With this established model, we can now calculate the elevation at any point for any given time by stitching together the elevations from the overlapping time series and computing a weighted average of the output.

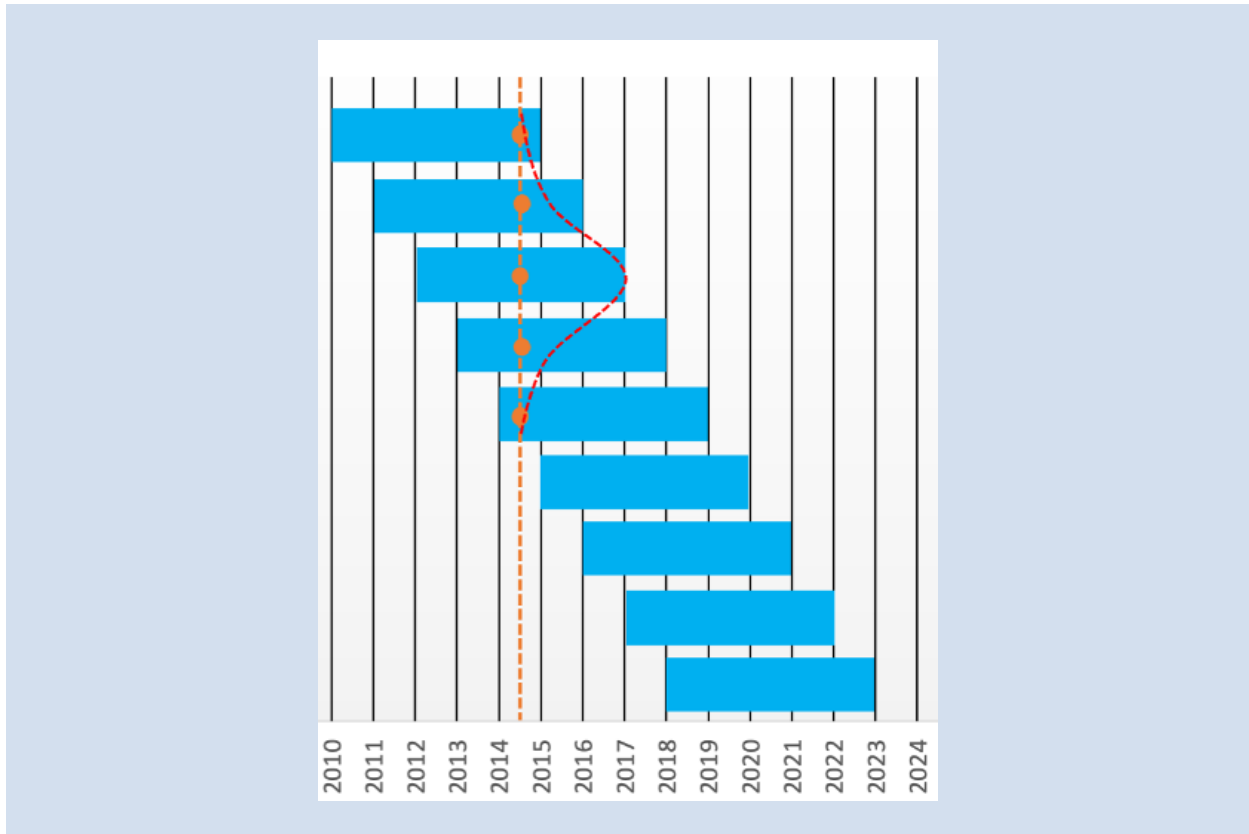


Figure 2.3: Sketch of the overlapping 5-year SEC data for the entire CryoSat-2 time period, where the vertical orange dashed line indicates a selected timestep where the 5 available models are used to compute the weighted average as shown by the red dashed line indicating the distribution of the weights.

2.5 Accuracy and performance

One benefit of using Kriging is the fact that it considers the error estimates of the point data and creates a grid of errors along with the SEC output grid. At grid points close to the input data locations (satellite tracks and crossovers) the SEC error is controlled by the input error estimates, and it then increases with distance to the input data locations. This was also the case for the previous products derived using collocation, so the performance of using Kriging will be similar.

2.6 Capabilities and known limitations

We refer here to Sections 2.6.3, 2.6.4, and 2.6.5 of (RD1) for a summary of the known limitations. When using Radar it measures the highest points inside the footprint, focusing on areas that are the highest points and not the topographically lower regions, which are known to be the fastest-changing regions. As new and improved relocation methods become available, we will incorporate them.



2.7 References

- Hudson, G., & Wackernagel, H. (1994). Mapping temperature using kriging with external drift: theory and an example from Scotland. *International journal of Climatology*, 14(1), 77-91.
- IMBIE Team (2019). Mass balance of the Greenland ice sheet from 1992 to 2018. *Nature*. <https://doi.org/10.1038/s41586-019-1855-2> ACCELERATED
- IMBIE Team (2018). Mass balance of the Antarctic Ice Sheet from 1992 to 2017. *Nature*, 558(7709), 219–222. <https://doi.org/10.1038/s41586-018-0179-y>
- Mottram, R., B Simonsen, S., Høyer Svendsen, S., Barletta, V. R., Sandberg Sørensen, L., Nagler, T., ... & Solgaard, A. (2019). An integrated view of Greenland ice sheet mass changes based on models and satellite observations. *Remote Sensing*, 11(12), 1407.
- Rastner, P., Bolch, T., Mölg, N., Machguth, H., Le Bris, R., Paul, F. (2012): The first complete inventory of the local glaciers and ice caps on Greenland. *The Cryosphere*, 6, 1483-1495. (doi:10.5194/tc-6-1483-2012).
- Royle, A. G., F. L. Clausen, and P. Frederiksen. "Practical Universal Kriging and Automatic Contouring." *Geoprocessing 1*: 377–394. 1981.
- Schröder, L., Horwath, M., Dietrich, R., Helm, V., Van Den Broeke, M. R., & Ligtenberg, S. R. (2019). Four decades of Antarctic surface elevation changes from multi-mission satellite altimetry. *The Cryosphere*, 13(2), 427-449.
- Simonsen, S. B., & Sørensen, L. S. (2017). Implications of changing scattering properties on Greenland ice sheet volume change from Cryosat-2 altimetry. *Remote Sensing of Environment*, 190, 207-216.
- Slater, Thomas (2019) Mapping Ice Sheet Elevation and Elevation Change Using CryoSat-2 Radar Altimetry. PhD thesis, University of Leeds.
- Slater, T., Shepherd, A., McMillan, M., Armitage, T. W., Ootosaka, I., & Arthern, R. J. (2019b). Compensating Changes in the Penetration Depth of Pulse-Limited Radar Altimetry Over the Greenland Ice Sheet. *IEEE Transactions on Geoscience and Remote Sensing*.
- Sørensen, L. S., Simonsen, S. B., Forsberg, R., Khvorostovsky, K., Meister, R., & Engdahl, M. E. (2018). 25 years of elevation changes of the Greenland Ice Sheet from ERS, Envisat, and CryoSat-2 radar



3 Ice Velocity (SAR)

3.1 Introduction

In Greenland Ice Sheet CCI+ the developments and further production for Ice Velocity (IV) build on the achievements of the Greenland Ice Sheet CCI Phase 1 and Phase 2 (2012-18). The major technical advancements emerging from GIS CCI were the development and implementation of an automatic system for the generation of ice velocity maps from repeat pass Copernicus Sentinel-1 (S1) Synthetic Aperture Radar (SAR) using offset tracking (OT). The annual velocity maps and unprecedentedly dense IV time series of outlet glaciers provide essential information for studying temporal fluctuations and long-term trends and provide key input for ice dynamic and climate modelling. The production of the annual maps is continued within the C3S services on ice sheets.

In Greenland Ice Sheet CCI+ IV is derived from both SAR and optical data using combinations of coherent and incoherent OT and InSAR. The main technical development on SAR derived IV in CCI+ Phase 1 was the extension of the IV processor for supporting Sentinel-1 TOPS mode InSAR, using ascending and descending crossing orbit pairs acquired in Interferometric Wide (IW) swath mode. The development significantly improved the accuracy of the ice velocity, in particular in the slower moving areas in the interior of Greenland. The main upgrade of the IV processing chain introduced in this phase of the project is the adaptation of the InSAR and OT algorithms to accommodate SAOCOM data in synergy with Sentinel-1 for improving ice surface velocity estimation in Greenland. For this, the existing InSAR and OT processing lines developed for other sensors in the previous CCI phases have been amended to accommodate SAOCOM data as well as the combination of SAOCOM and Sentinel-1.

This chapter provides the Algorithm Theoretical Basis for IV, building on the ATBD of GIS CCI (RD1) and GIS CCI+ Phase 1, and provides an overview, description, and update of the scientific background, the IV retrieval algorithms, input, and output data, expected accuracy and performance, and capabilities and known limitations.

3.2 Review of scientific background

The principal method for generating velocity fields on glacier and icesheet surfaces is Offset Tracking (OT). OT refers to several related methods that include amplitude tracking or feature tracking, coherence tracking and speckle tracking. Feature tracking uses cross-correlation of image patches to find the displacement of surface features such as crevasses or rifts and edges, that move with the same speed as the ice and are identifiable on two co-registered amplitude images, and subsequently ice flow velocity. In coherence tracking (SAR only), the offset which maximises the interferometric coherence within a certain window size is determined and used to derive the ice velocity. Speckle tracking (SAR only) uses the cross-correlation function of radar speckle patterns, rather than visible features, to derive ice flow velocity.

Spaceborne methods for measuring ice velocity have focused primarily on the above mentioned methods applied to both optical and SAR sensors (Joughin et al, 2010; Nagler et al, 2015; Mouginot et al, 2017; Joughin et al, 2018). The use of SAR data has several advantages over optical imagery, including the ability to observe through cloud cover and during the polar night. Another advantage is that penetration of radar waves into the upper snow layers can reveal shallow sub-surface or snow-covered features that can be successfully tracked but are usually hidden in optical imagery. Also, there is a stronger contrast between different types of ice (e.g. sea ice and ice shelves) in SAR imager that are difficult to distinguish in optical imagery, allowing ice shelf edges to be tracked more easily.

OT has been extensively applied to the Greenland and Antarctic Ice Sheets and has proven to be efficient for large-scale continuous monitoring (Nagler et al, 2015; Joughin et al, 2018). However, SAR offset-tracking methods are amplitude-based and do not exploit the full information provided by SAR images. Their accuracy



is primarily controlled by the spatial resolution (i.e., pixel posting) of the sensor and reaches at best some meters per year. In contrast, differential SAR interferometry (InSAR) can reach a precision of one to two orders of magnitude better than OT. Even though InSAR has proved efficient for ice monitoring, it has been scarcely used for large scale or continuous monitoring of ice sheets. InSAR requires measurements from crossing ascending and descending orbits to determine the different components of the velocity vector (Joughin, 1998; Gray, 2011). In addition, the application of InSAR also requires a good level of coherence between repeat image pairs to generate suitable interferograms. The Greenland Ice Sheet is subject to highly variable meteorological conditions, resulting in rapid temporal decorrelation of the radar signal phase impairing the comprehensive application of InSAR. For this reason, InSAR is in general applied to complement OT measurements (Joughin, 2002; Rignot et al, 2011; Mougnot et al, 2012). OT is less sensitive or insensitive to temporal decorrelation of the radar phase signal, albeit at a lower accuracy of velocity. In areas with distinct and stable surface features, as common on mountain glaciers and outlet glaciers of ice sheets, coherence of the repeat-pass SAR data is not required because the cross-correlation of image-templates is based on the amplitude signal.

Sentinel-1 has significantly increased the SAR coverage in the polar regions, with routine 6- and 12-day coverage of the GIS margins and peripheral glaciers as well as smaller Arctic ice caps and glaciers. Before the launch of Sentinel-1, crossing orbit SAR data were not systematically acquired and not always with a satisfactory temporal baseline. The unprecedented data set provided by the Sentinel-1 satellites opened the possibility to improve IV measurements over Greenland by applying InSAR in a more systematic fashion. Nevertheless, some glacier areas are covered by only one single Sentinel-1 track, making it impossible to derive the full velocity vector from InSAR only and reducing the applicability of InSAR for ice velocity retrieval. However, if the flow direction is known and assumed constant, InSAR measurements can be used to retrieve the magnitude of the velocity vector. In contrast to InSAR, OT can derive velocity vector components from a single acquisition geometry. Even though OT is much less accurate than InSAR when applied to a single pair of images, it reaches a satisfactory accuracy when stacking measurements over longer periods. To improve existing maps and maximize the synergy of InSAR and OT, it is possible to combine the flow direction derived from OT with the InSAR line-of-sight (LoS) velocity measurements, assuming stability of the flowlines over time (Nagler et al., 2022). With this approach, the velocity field can be determined, wherever single- or multi-track InSAR measurements are available, except on the ice divide where the flow vector is null.

Recently, the loss of Sentinel-1B has further hampered the application of InSAR due to the reduced repeat-pass period from 6 to 12 days as well as the reduced coverage of crossing-orbits pairs. 8-day repeat-pass L-Band SAR data over Greenland are since 2021 also acquired by SAOCOM A/B SAR mission as a background mission (i.e. without systematic acquisition plan) and is tested here as a possible way to fill in this gap. The prime payload of the dual satellite constellation is an L-band polarimetric SAR instrument, managed and operated by CONAE (Comisión Nacional de Actividades Espaciales - Argentina's Space Agency). By using L-Band SAR data the use of the InSAR method can be extended to cover faster moving areas than possible with C-band (Sentinel-1). L-band data have a reduced fringe frequency in shear zones and fast-moving areas, enabling more reliable phase unwrapping so that the InSAR method can also be applied in zones where Sentinel-1 data decorrelate. Additionally, the L-band signal coherence is less affected by variable surface conditions than C-band. Consequently, further improvement for ice velocity monitoring can be expected from the synergy of C-band and L-band InSAR data, as rendered possible by combining Sentinel-1 and SAOCOM A/B. Using SAOCOM data we focus the work in Phase 2 of GIS CCI+ on the developments of methods for combining L- and C-Band interferometric data for ice velocity monitoring using both InSAR and OT.

3.3 Algorithms

3.3.1 SAR Offset Tracking

We provide here a brief summary of the OT processor, for further details the reader is referred to (RD1). Figure 3.1 shows the high-level flow chart for offset tracking to retrieve maps of icesheet surface velocity using repeat-pass SAR images, as implemented in ENVEO's SAR processing system. The generalised processing line for offset-tracking could be readily adapted to accommodate also SAOCOM data. The software contains three main modules.

Within the IV module SAR data and orbit data are imported into the system, SAR images are co-registered and velocity maps are generated for pairs of repeat pass data of the same track. The importer imports the repeat-pass SAR data and corresponding metadata describing SAR, focussing, orbit and attitude information. The coregistration performs the alignment of the second (slave) image with the first (master) image, whereby the master image defines the geometry. Geometric DEM-assisted coregistration is applied, computing for each pixel of the master image acquisition the corresponding pixel in the slave scene and storing the relative shift in the shiftmap file. In the case of accurate orbit and attitude information, as provided by TerraSAR-X, TanDEM-X and Sentinel-1, this co-registration step is sufficient for proceeding with the ice velocity retrieval. For older SAR systems or systems with less accurate orbits (e.g. SAOCOM), in addition an iterative cross-correlation over stable terrain or OT assisted co-registration (using a long-term averaged map) is needed in order to improve the estimate of the local shift in range and azimuth for the slave relative to the master image. The IV generation performs advanced iterative OT to generate detailed displacement maps in SAR geometry. The tracks are geocoded into the common map projection of the output grid, providing observations of slant range displacement and azimuth for each track separately. The local incidence and heading angle are calculated using the annotated image and orbit parameters and a DEM as input.

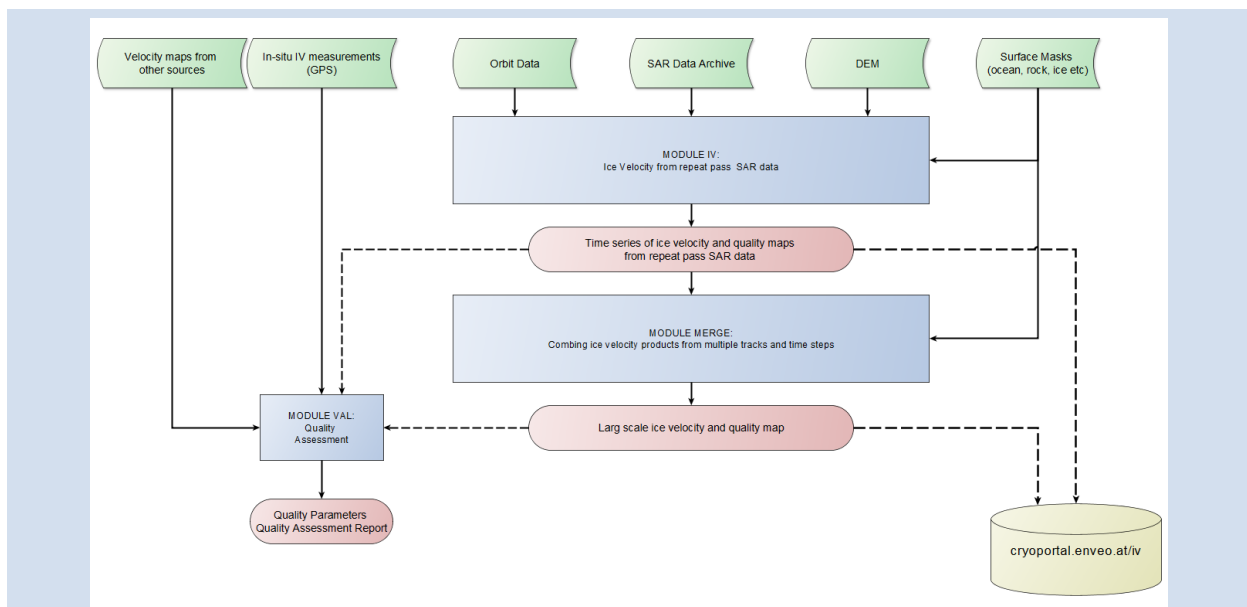


Figure 3.1: High-level flow chart of the IV processing system. Green – input data, Blue – processing modules, Red - product and intermediate products, Yellow – product data base.

The Merge module combines IV products from different tracks and image pairs (with various repeat intervals) over a specified time span (i.e. 1 year) to generate a regional ice velocity map, applying a weighted average approach. The combination of displacement observations of multiple tracks applies a weighted least squares model to fit the multiple observed displacements according to:

$$y = Ax + \epsilon$$

where x is the horizontal velocity vector (in local Easting/Northing coordinates), y is a vector with the observed velocities (in slant range/azimuth), A is the matrix projecting the horizontal velocity to slant range/azimuth geometry, and ϵ is a noise vector.

Lastly the Validation module facilitates quality assessment of the IV products, by automating various standard validation tests, including internal consistency checks and intercomparisons with independent data sets (e.g. in-situ GPS, or other published velocity maps).

3.3.2 SAR Interferometry

The interferometric phase ϕ difference between two SAR images acquired at different times is the sum of multiple components:

$$\phi = \phi_{flat} + \phi_{topo} + \phi_{displ} + \phi_{atm} + \phi_{iono} \quad (3.1)$$

where ϕ_{flat} is the flat-earth phase, ϕ_{topo} is the topographic phase, ϕ_{displ} is the phase due to ground displacement along the sensor line-of-sight (LOS), ϕ_{atm} is the atmospheric phase and ϕ_{iono} is the ionospheric phase. To estimate ice velocity, the displacement phase component must be isolated. This means that DInSAR processing includes removal of flat-earth and topography. Under the assumption that the atmosphere and the ionosphere are in a similar state for both acquisitions, the atmospheric and ionospheric components may be neglected.

The interferometric phase is computed as the argument of the product of the master image with the complex conjugate of the slave image. The result is a wrapped version of the absolute phase, with values ranging between $-\pi$ and π . The interferogram must be unwrapped to retrieve the absolute phase. However, phase unwrapping algorithms usually estimate the unwrapped phase of a pixel with respect to the phase of its neighbours. As a result, the unwrapped phase is shifted by an unknown amount with respect to the absolute phase. For this reason, the unwrapped phase must be further calibrated: the knowledge of points with zero velocity is used to determine the phase shift to be applied.

Once calibrated, the absolute phase must be converted into LOS velocity: LOS displacement is obtained by applying a $\frac{\lambda}{4\pi}$ conversion factor, with λ being the radar wavelength, and the velocity is calculated as the displacement per day, knowing the temporal baseline of the interferometric couple.

When interferometric processing is applied to a single geometry (i.e., to a given track, ascending or descending, with given heading and incidence angles), it only measures the displacement projected onto the line-of-sight. For calculating the 3-D velocity, LOS measurements from different geometries must be merged.

Because interferometric measurements are prone to decorrelation, interferometry can only perform efficiently over ice bodies with stable conditions between the acquisitions: no melting, same type of snow surface, etc. Moreover, interferometry performs better on slow-moving areas: indeed, ice velocity can reach very large values (e.g., meters per day) causing important displacements even over a few days. Such displacements cannot be measured with interferometry as they result into aliased fringes in the interferogram that cannot be unwrapped.

The high-level processing line for InSAR is pictured in Figure 3.2. This processing line is originally designed for Sentinel-1 TOPSAR acquisitions (cf. IW – Interferometric Wide mode), but it can be easily modified to suit other sensors and acquisition modes. Adaptation of the processing line for SAOCOM data focus on handling large baselines and automatization of co-registering. SAOCOM data, by combining orbital data, a DEM and refinement using local matching, which is needed due to the reduced quality of the orbital state vectors.

In S1 TOPSAR mode, the antenna is sequentially steered from the aft to the fore, so that the ground is not continuously scanned. The imaged area is scanned as 3 sub-swaths (or 5 in EW – Extended Wide mode), which are divided into slightly overlapping bursts. The interferometric processing, including co-registration, interferogram generation, phase flattening and topography removal is performed on each burst separately. The burst interferograms are then mosaicked at the debursting step.

The subsequent processing is performed at the debursted level. Once the interferogram generated, the phase must be unwrapped and calibrated. Afterwards, it can be converted into LOS velocity. In ENVEO implementation, the LOS velocity is also projected onto the horizontal plane. Images of horizontally projected LOS velocity are produced for different tracks and dates, and they are all geocoded on a common projection grid. Finally, these maps are used for inverting the system described below and for estimating the components of the horizontal velocity. The final product is a measurement of the east-west and north-south component.

In case of another acquisition mode than TOPSAR (e.g., Stripmap mode as used for SAOCOM), the processing line is similar but the debursting step can be skipped as we are directly working with large-scale images. A short description of each module is provided below.

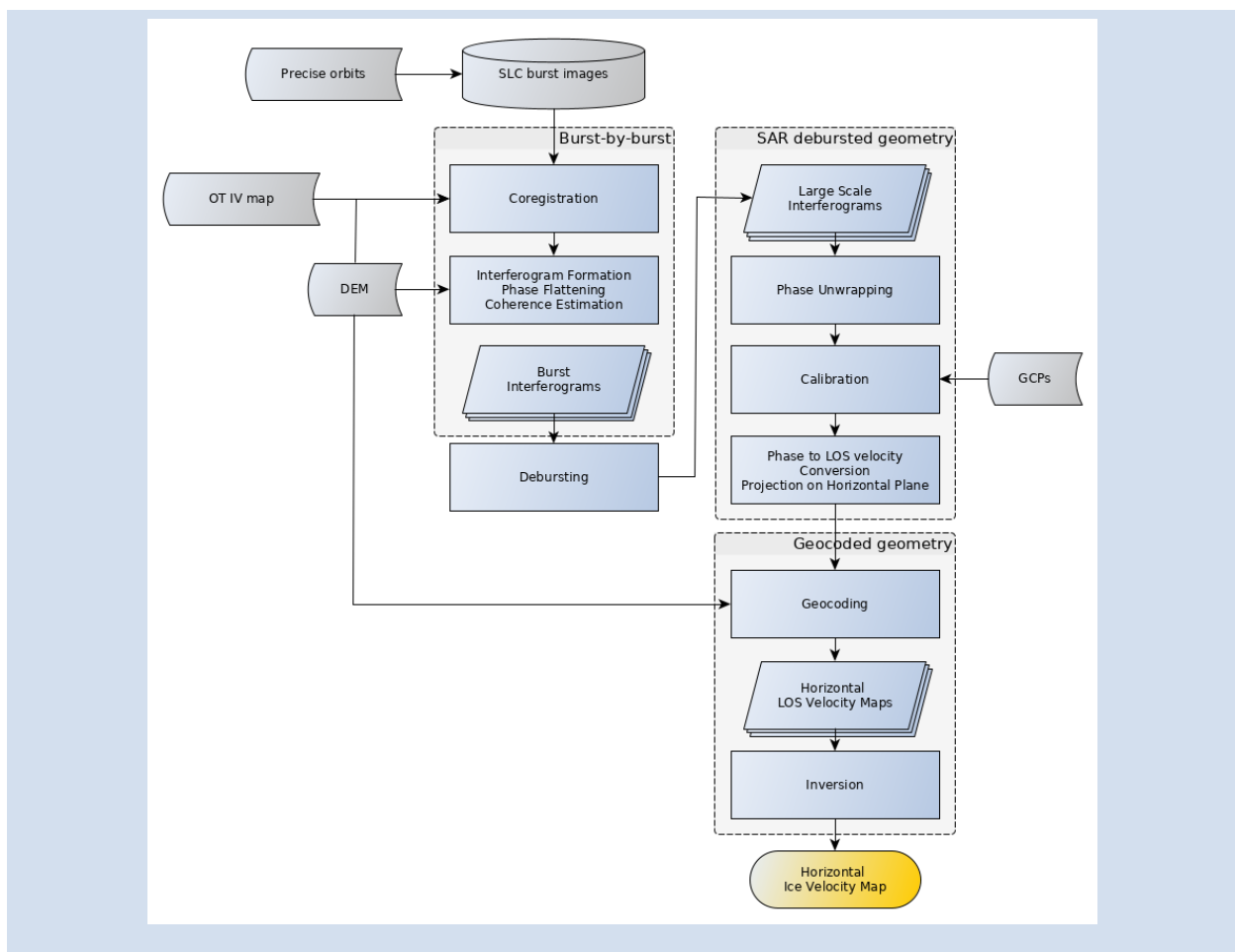


Figure 3.2: Interferometry processing for ice velocity (IV) map generation. The flowline is dedicated to Sentinel-1 TOPSAR acquisitions. SLC – Single-Look Complex. OT – Offset Tracking. LOS – Line-of-sight. GCP – Ground Control Point. For SAOCOM SM the flowline is similar but the debursting step is not necessary.

- **Coregistration:** For S1 co-registration is performed at the burst level, but is otherwise similar as for SAOCOM. Precise orbits and a Digital Elevation Model (DEM) of the area are used to determine the shifts

between the master and slave geometry. In S1 TOPSAR mode, because of the steering of the antenna, the line-of-sight changes from one burst to the other at the overlapping area. In case of motion in the azimuth direction, the varying line-of-sight introduces phase discontinuities at burst overlap. We correct this effect by accounting for the average ice motion: using the IV map from Offset Tracking, we update the co-registration map with the local displacements between the master and slave acquisition dates. The co-registration module also includes the resampling step. For Sentinel-1 data, the steering of the antenna introduces a Doppler frequency variation in the azimuth direction. Therefore, the co-registration of Sentinel-1 images includes de-ramping and re-ramping of complex images in the azimuth direction respectively before and after interpolation.

- **Interferogram formation:** the interferometric phase is calculated for each master-slave burst pair. The flat-earth phase is estimated and removed. The topographic phase is estimated from an external DEM and subtract from the interferogram. The output is the wrapped displacement phase.
- **Debursting:** burst interferograms are mosaicked together using the range and azimuth time information of each pixel. Additional smoothing at the burst overlap can be performed to removed phase jumps due to changing orientation of the line-of-sight. These phase jumps are already significantly reduced by accounting for ice motion at the co-registration step. This step is only needed for S1 TOPS mode data and not for SAOCOM SM data.
- **Phase unwrapping:** phase unwrapping of very large interferograms can either be handled with SNAPHU, applying a tiling strategy (Chen and Zebker, 2002), or with an iterative least-square phase unwrapping.
- **Calibration:** calibration is usually performed by using zero-velocity ground control points (GCPs). However, zero velocity GCPs are not always available for all tracks covering the Greenland Ice Sheet. Therefore, we select low velocity as GCPs and perform calibration by adjusting their phase to the average velocity provided by the IV map from OT. For this purpose, the IV map must be projected into SAR geometry, multiplied by the temporal baseline to yield the displacement, and converted into phase. A low order polynomial function is fitted to the difference between the IV phase from OT and InSAR of slow-moving points. If the polynomial order is 0, then calibration function consists in a simple constant shift. If the order is equal to 1 in azimuth and range directions, then the calibration function consists in a plane and accounts for possible orbits errors in the phase.
- **Phase-to-velocity conversion:** the calibrated absolute phase is converted into LOS velocity (i.e., displacement per day) by applying pixelwise the conversion factor $\frac{\lambda}{4\pi\Delta t}$, with λ being the radar wavelength and Δt the temporal baseline (usually provided in days). At this stage, the LOS velocity is further projected onto the horizontal plane. Projection onto the horizontal plane is obtained by dividing LOS velocity by the factor $\sin \theta$, where θ is the local incidence angle. Projection onto horizontal eases the final inversion, as all velocity vectors are already on a common plane and the system to be inverted only needs to account for heading angles.
- **Geocoding:** horizontally projected LOS velocity from all dates and tracks are geocoded on a common projection grid.
- **Inversion:** this step is meant to determine average horizontal velocity components. Provided that velocity measurements from at least two different geometries (i.e., two different heading angles) are available for a given point, the east-west and north-south velocity components can be determined. For this purpose, the system to be inverted is:

$$V_{LOS} = AV \quad (3.2)$$

where V_{LOS} is the N-dimensional vector of the measured LOS velocities projected on the horizontal plane, A is the matrix with dimensions N x 2 projecting the horizontal velocity on the LOS and V is the 2-dimensional vector of horizontal velocity components. Let us consider N horizontally projected LOS velocity measurements $v_{los_i}^H$. The index i refers to the geometry of acquisition and the corresponding heading angle ϕ_i . The system can be explicitly written as:

$$\begin{bmatrix} v_{los_1}^H & v_{los_2}^H & \vdots & v_{los_N}^H \end{bmatrix} = \begin{bmatrix} \cos \phi_1 & \sin \phi_1 & \cos \phi_2 & \sin \phi_2 & \vdots & \cos \phi_N & \sin \phi_N \end{bmatrix} \begin{bmatrix} v_E & v_N \end{bmatrix} \quad (3.3)$$

Where v_E and v_N are respectively the east and north components of the horizontal surface velocity. These components can be determined only where data with crossing orbits (e.g. ascending SAOCOM – descending Sentinel-1) are available.

3.3.3 Combined InSAR and OT

The combined approach of InSAR and OT flow direction is described in Fig. 3.3. In this flowchart, the InSAR processing corresponds to the interferometric processing for ice velocity retrieval described in section 3.3.2. In parallel to the interferometric processing, the flow direction is derived from the OT multiannual velocity map. The flow direction is computed as the angle between the velocity vector and the east direction.

The line-of-sight (LOS) velocity maps resulting from the interferometric processing and the OT derived flow direction map are combined in the inversion process, which consists of a weighted least squares linear regression. Since the LOS velocity data points are the projected measurements of the velocity vector, they have a linear dependence on the projection coefficients and this linear dependence has a slope corresponding to the velocity magnitude. The projection coefficients are defined by the flow direction and the InSAR geometry (incidence and heading angles). Therefore, the inversion process enables estimating the velocity magnitude, which is finally projected on the x and y direction of the ice flow for computing the x-, y- and z-components of the velocity field.

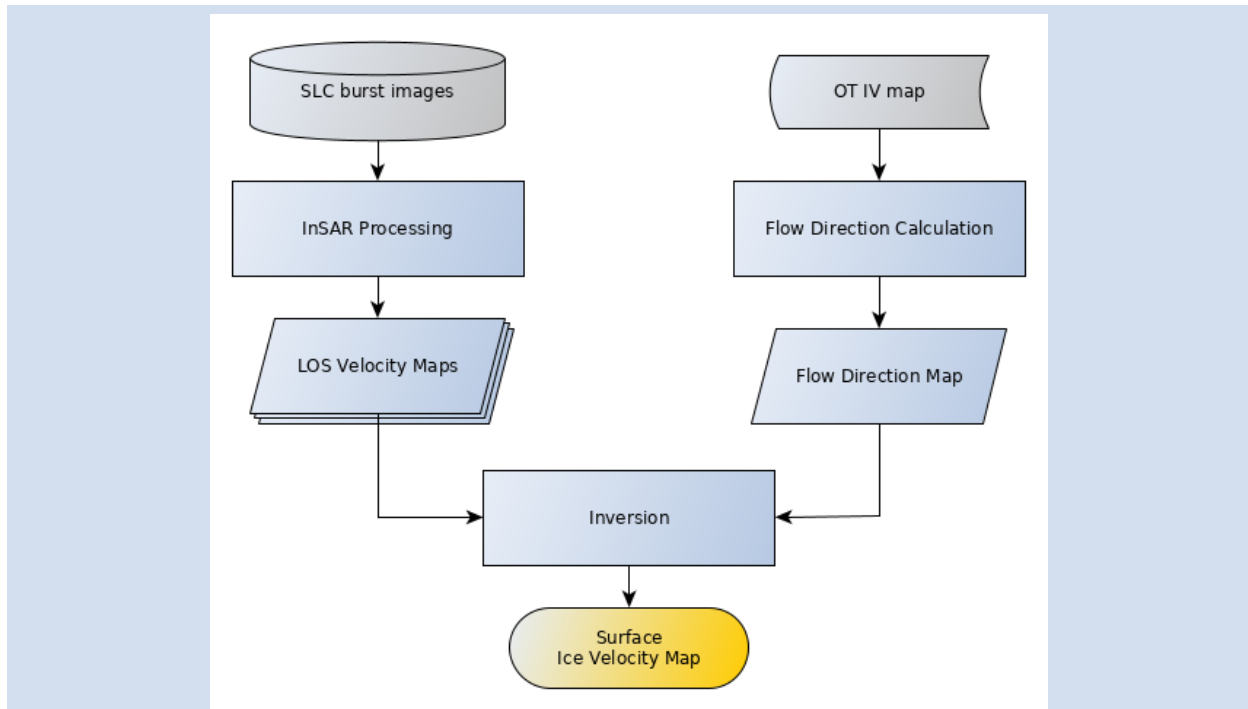


Figure 3.3: Combined approach of SAR interferometry and offset-tracking for ice velocity retrieval.

3.3.4 Remarks

The current processing is meant to determine horizontal ice velocity. Projecting the LOS velocity onto the local slope instead of the horizontal plane (cf. surface-parallel flow), 3-D surface velocity could be determined with a similar approach. It would however require slight changes into the current implementation of the flowline. Given that interferometry performs better over slow-moving ice bodies, such the interior of the Greenland Ice Sheet where the topography is rather flat, no significant difference is expected from the two approaches.

3.4 Input data and algorithm output

3.4.1 Input Data

Input data for IV products generated in CCI+ Phase 2 consists of both Sentinel-1 and SAOCOM SLC images. Because SAOCOM has a much larger orbital tube and generally no burst synchronisation in TOPSAR mode we use SAOCOM StripMap (SM) data. Given that ice motion can already cause very large displacements over short intervals, in general only short temporal baselines are selected (6 and 12 days for Sentinel-1, 8 or 16 days for SAOCOM), but for SAOCOM we also test larger temporal baselines up to 32 days. Moreover, the changing state of the ice during the melting season can cause decorrelation and prevent InSAR measurements. Therefore, we mainly focus on the winter season, but this is primarily dictated by the availability of suitable repeat-pass SAOCOM data which is sparse in Greenland to date.

For Sentinel-1 TOPSAR acquisition, the input data are pairs of master and slave bursts in SLC format. In best cases, Sentinel-1 has a revisit cycle of 6 days (currently 12 days). Sentinel-1 IW and EW TOPS Mode SLC Products, as provided by ESA, consist of 3 or 5 sub-swaths, each consisting of a series of bursts, each burst has been processed as a separate SLC image. By importing Sentinel-1 SLC IW/EW SLC products into the software system each burst is extracted separately and the corresponding metadata information is stored in separate files. We take care to assign correct azimuth timing and slant-range timing for each burst, which is needed for debursting and for co-registering corresponding bursts of repeat pass acquisitions. Within the IV

processor software an imported burst can be treated the same way as a frame of Stripmap Mode SAR data (e.g. SAOCOM), except for the phase de-ramping needed during the resampling step.

The SAOCOM-1 SAR mission is composed of two satellites (SAOCOM-1A and 1B) with L-band polarimetric SAR launched in 2018 and 2020 respectively. The mission is managed and operated by the Comisión Nacional de Actividades Espaciales (CONAE). SAOCOM provides L-Band SAR data over glaciers and ice sheets as a background mission, without systematic acquisition plan, and has a revisit time of 16 days (with 1 satellite) and 8 days (with the constellation). There are two main operational modes, Stripmap (SM) and TopSAR, operating with 9 beam modes (S1-S9) with incident angles ranging from 20-50 degrees (<https://earth.esa.int/eogateway/missions/saocom>).

Precise orbits of Sentinel-1 acquisitions are provided by ESA as independent products. These orbits have 5 cm accuracy in the along-track, across-track and vertical directions and are available 20 days after the acquisition. Orbits for SAOCOM are provided by CONAE and come with the product (OFFLINE_FAST) and are provided after 2 days, the accuracy is listed as 70 m.

The IV processor can be supplied with a digital elevation model in any supported projection (latitude-longitude, UTM, Polar Stereographic, etc.). The DEM is projected into the SAR geometry by the interferometric processor.

3.4.2 Algorithm output

The output product is a map of the east and north of components of horizontal ice velocity provided in meters per day. The velocity grid for a single image pair represents the average ice surface velocity over the respective repeat pass period. The generation of regional ice velocity maps requires the combination of results from several tracks. These maps form the input for further derived monthly and annually averaged maps.

3.5 Accuracy and performance

A detailed error analysis is outside the scope of this document, but the processing line has been tested over Petermann Glacier in northern Greenland as well as on NEGIS (central Greenland). For these preliminary tests, we intercompare the ice velocity derived from SAOCOM OT and SAOCOM/S1 InSAR with long-term averaged Sentinel-1 derived OT results.

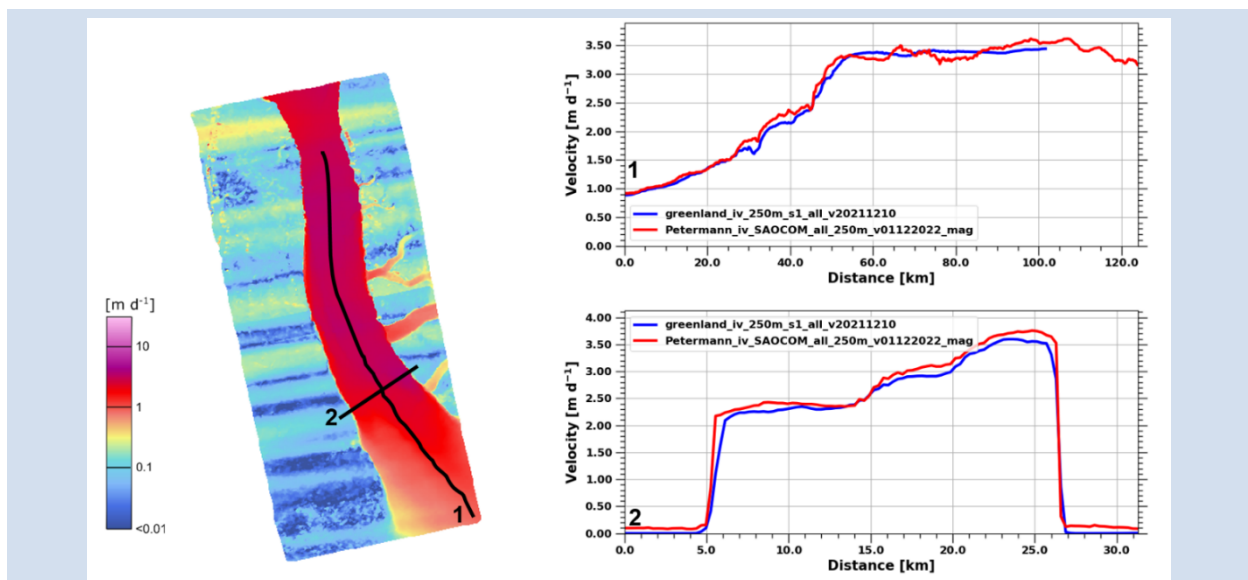


Figure 3.6: Ice velocity map of Petermann Glacier derived from SAOCOM OT (left) and velocity profiles showing an intercomparison with Sentinel-1 derived ice velocity along two profiles (right). The location of the profiles is indicated by the numbers and black lines in the left panel.

For Petermann Glacier we processed a selection of SAOCOM image pairs with an 8-day temporal baseline acquired on 2022/02/16 and 2022/02/24 (track 7) using offset tracking. For visualization purpose, we converted the 2-D horizontal velocity into magnitude. The result is shown in Figure 3.6, and is compared with Sentinel-1 OT IV measurements from a long term averaged map. The agreement between both is rather good, but as can be seen the IV map suffers from streaks caused by ionosphere.

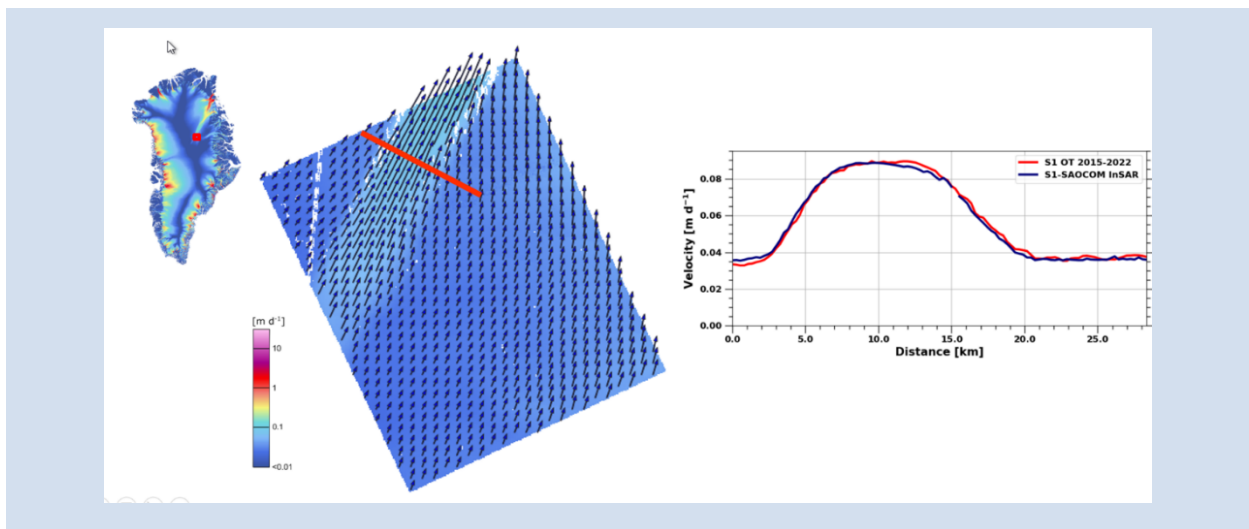


Figure 3.7: Comparison between IV measurements from SAOCOM/Sentinel-1 InSAR and Sentinel-1 OT. Left: Velocity magnitude along NEGIS with flow vectors showing direction of flow (inset shows location in central Greenland). Right: velocity profile showing InSAR (blue) and OT (red) derived ice velocity along a cross profile (red line in left image).

On NEGIS we generated an ice velocity map based on crossing orbit InSAR using both SAOCOM (ascending) and Sentinel-1 (descending) passes. Despite that the SAOCOM image pair has a temporal baseline of 32-days (2022/04/21-2022/05/23) the coherence is very good, enabling successful unwrapping and providing a complete LoS velocity map for the scene. Figure 3.7 shows the InSAR derived ice velocity map and a comparison between SAOCOM/S1 InSAR and S1 OT along a cross profile. As can be seen the agreement between the two is very good. The InSAR IV map does not show ionospheric streaks.

3.6 Capabilities and known limitations

OT accuracies depend on various factors, including on the level of coherence, on the correlation window size (Bamler and Eineder, 2005) as well as on the type of features that are being tracked. In addition, ionospheric scintillations can have a large impact on offset tracking by causing azimuth shifts that are introduced by the fluctuating electron density along the sensor path (see Fig. 3.4). Misregistration is not a problem, but the large azimuth shifts are interpreted as ice motion and observed offsets can exceed the azimuth pixel size. There are several options to correct for ionospheric artefacts. Over the interior parts of the ice sheets (where the velocities are stable in time) image stacking has usually been applied for the shifts in azimuth and range of the individual image pairs. The use of crossing tracks (ascending/descending) helps reducing ionospheric offsets in case of offset-tracking by putting larger weight on the LOS components of the displacement measurements.



Compared to the Offset Tracking approach that yields at best an accuracy of some tens of centimetres, InSAR has the ability to estimate ground displacements with an accuracy better than a centimetre. However, InSAR performance for measuring ice motion is limited by a number of factors. The main limitations are:

- Ionosphere: at high latitude, the total electron content (TEC) of the ionosphere is very likely to vary (both in space and time) between two acquisitions. Different TEC introduce a phase delay related to the path travelled through ionosphere, which can bias or mask the ice motion signal.
- Change in snow conditions: if snow surface undergoes change such as melting or snowfall, the change in the surface state can cause decorrelation. For this reason, InSAR shows better performance during the wintertime, during which snow conditions are more stable.
- Fast-moving areas: large displacements cause aliasing or decorrelation in interferograms. For this reason, fast-moving ice areas cannot be efficiently covered by Sentinel-1 C-Band data with 6-day revisit time. SAOCOM, operating at L-Band, on the other hand can cover also faster moving areas with an 8-day revisit time.

3.7 InSAR Line-of-sight velocity prototype product

The InSAR Line-of-sight velocity product is based on intermediate products generated during the InSAR velocity processing, and thus the algorithm is essentially the same as described in section 3.3.2, except that the line-of-sight velocity is output right after the Geocoding step and before the Inversion step. The geocoded LoS velocity maps from several acquisitions on the same track are then stacked to form a timeseries, and the pixelwise median of the timeseries is subtracted, such that the output product is the LoS velocity anomaly, which can reveal small-scale rapid variations related to e.g. subglacial hydrological phenomena, as described in (Andersen, 2023).

3.8 References

- Andersen, J. K., Rathmann, N., Hvidberg, C. S., Grinsted, A., Kusk, A., Merryman Boncori, J. P., & Mouginot, J. (2023). Episodic subglacial drainage cascades below the Northeast Greenland Ice Stream. *Geophysical Research Letters*, 50, e2023GL103240. <https://doi.org/10.1029/2023GL103240>
- Bamler, R. and Eineder, M. (2005): Accuracy of differential shift estimation by correlation and split-bandwidth interferometry for wideband and delta-k SAR systems, *IEEE Geosc. Rem Sens. Lett.* 2, 151-155.
- Chen, C. W. and Zebker, H. A. (2002), Phase unwrapping for large SAR interferograms: Statistical segmentation and generalized network models", *IEEE Transactions on Geoscience and Remote Sensing*, vol. 40, pp. 1709-1719.
- Gray, L. (2011), Using multiple RADARSAT InSAR pairs to estimate a full three-dimensional solution for glacial ice movement. *Geophysical Research Letters*, 38(5).
- Joughin, I., Kwok, R. and Fahnestock, M.A. (1998) Interferometric estimation of three-dimensional ice-flow using ascending and descending passes. *IEEE Trans. Geosc. and Remote Sens.*, 36(1), 25-37.
- Joughin, I. (2002). Ice-sheet velocity mapping: a combined interferometric and speckle-tracking approach. *Annals of Glaciology*, 34, 195-201.
- Joughin, I., Smith, B. E., Howat, I. M., Scambos, T. and Moon, T. (2010). Greenland flow variability from ice-sheet-wide velocity mapping. *Journal of Glaciology*, 56(197), 415–430. doi:10.3189/002214310792447734
- Joughin, I., Smith, B. E. and Howat, I. (2018), Greenland Ice Mapping Project: ice flow velocity variation at sub-monthly to decadal timescales, *The Cryosphere*, 12, 2211–2227, <https://doi.org/10.5194/tc-12-2211-2018>, 2018.



Mouginot, J., Rignot, E. and Scheuchl, B. (2019). Continent-wide, interferometric SAR phase, mapping of Antarctic ice velocity. *Geophysical Research Letters*. doi:10.1029/2019gl083826

Mouginot, J., Rignot, E., Scheuchl, B. and Millan, R. (2017), Comprehensive Annual Ice Sheet Velocity Mapping Using Landsat-8, Sentinel-1, and RADARSAT-2 Data. *Remote Sens.* 2017, 9, 364.

Mouginot, J., Scheuchl, B. and Rignot, E. (2012), Mapping of Ice Motion in Antarctica Using Synthetic-Aperture Radar Data. *Remote Sens.* 2012, 4, 2753-2767.

Nagler, T., Rott, H., Hetzenecker, M., Wuite, J. and Potin, P. (2015), The Sentinel-1 Mission: New Opportunities for Ice Sheet Observations. *Remote Sens.* 2015, 7, 9371-9389.

Nagler, T., Libert, L., Wuite, J., Hetzenecker, M., Keuris, L., Rott, H.: Comprehensive Ice sheet wide velocity mapping combining SAR interferometry and offset tracking. *Proc. IGARSS 2022*, pp. 3888-3891, 10.1109/IGARSS46834.2022.9884206.

Rignot, E., Mouginot, J. and Scheuchl, B. (2011), Ice flow of the Antarctic Ice Sheet. *Science*, 333(6048), 1427–1430. <https://doi.org/10.1126/science.1208336>



4 Ice Velocity (Optical)

4.1 Introduction

Based on the User Requirement Document (URD), the IV algorithms must be able to generate ice-sheet maps of mean-seasonal velocities as well as time-series of velocity measurements. The term velocity should be understood as "velocity vector" since users require all its components to be measured. These and other requirements are summarized in Table 4.1, where also the Global Climate Observation System (GCOS) requirements are reported for convenience. The core measurement techniques for IV are quite well established and the one used for the retrieval of the IV from optical imagery is shortly described in Section 4.3. To meet the requirements listed in Table 4.1, an algorithm combining these core-techniques is required.

Table 4.1: Overview of IV requirements

Parameter	URD	GCOS (2022)
Velocity components	Cartesian (ENU)	-
Spatial coverage	Whole ice-sheet*	-
Minimum spatial resolution	100 m-1 km	1000 m
Optimum spatial resolution	50-100 m	50-100 m
Minimum temporal resolution	Annual	Annual
Optimum temporal resolution	Monthly	Monthly
Minimum accuracy	30 m/y	10 m/y

* Note: Optical IV ECV is produced for 9 large outlet glaciers only. Indeed, a large amount of science users are interested in these outlet glaciers because they represent the outlet conduits for the majority of ice sheet mass loss.

4.2 Review of scientific background

Space-borne IV measurements are currently carried out with SAR or with optical sensors. For the calculation of optical IV, measurement techniques based on optical imagery are offset-based. The main characteristics of offset tracking methods, and particularly feature-tracking one, which is the one used to produce the CCI Optical IV ECV, is described in the following sub-sections.

4.3 Algorithm

The optical IV ECV produced within the CCI project is based on the offset tracking method, and more specifically feature-tracking. The term offset tracking refers to a family of methods, which includes speckle tracking (Gray et al. 2001; Joughin, 2002), coherence-tracking (Derauw, 1999) and feature-tracking (Lucchitta et al., 1995; Michel and Rignot, 1999; De Lange et al., 2007). The same approach is applicable to both SAR and optical images. While SAR has the advantage of an active sensor that is not affected by solar illumination (day/night) or cloud coverage, the optical IV products are indeed dependent on these conditions. However, IV products generated from high-resolution allows for optical data to fill gaps in SAR IV products generated during summer in areas with surface melt and particularly along the margins.

The feature-tracking algorithm used to calculate optical IV CCI ECV is based on IMCORR (Fahnestock et al. 1992; Scambos et al. 1992), but updated to a modernized framework. The algorithm determines offsets by cross-correlating small sub-scenes (here referred to as "chips") from two input images. Behind the scenes a fast Fourier transform is utilized to calculate the normalized cross-correlation (Berenstein, 1983).



4.3.1 The Optical IV feature tracking algorithm

The core of the optical IV product algorithm is the offset tracking, which uses a feature tracking algorithm that takes a pair of optical images of the same region of interest. Having had the pair of images coregistered and pre-processed, the images are gridded, with one image designated as the *reference* image, and another the *search* image. When setting up a grid of a given grid spacing (e.g., a grid point at every 10 pixels), the algorithm will try to find the region of maximum correlation of the reference image within the search image. As previously mentioned, the normalized cross-correlation (NCC) will be used to track the offset correlations. The NCC will be performed between the reference chip (50 by 50 pixels) and the search chip (100 by 100 pixels), i.e., the smaller sub-scene in the reference image will be compared to the larger sub-scenes in the search image. The output will be an image over the search area of the *correlation strength*. The maximum peak in this search area image will indicate the offset or ice sheet displacement in pixels. To account for the fact that the maximum correlation peak might not be exactly at a pixel point, the correlation surface will be fitted to an elliptical paraboloid, and the maximum is instead extracted from this function.

The output of the feature tracking will have the units of meters per day in the north and east directions between the input image pairs, as well as the root-mean-square (RMS) of them.

4.3.2 Processing pipeline

The processing pipeline is split into several steps, and stringed together using S&T's in-house pipeline framework tool Dagger, requiring only a configuration file as user input. The steps are explained below, and can be viewed in Figure 4.1.

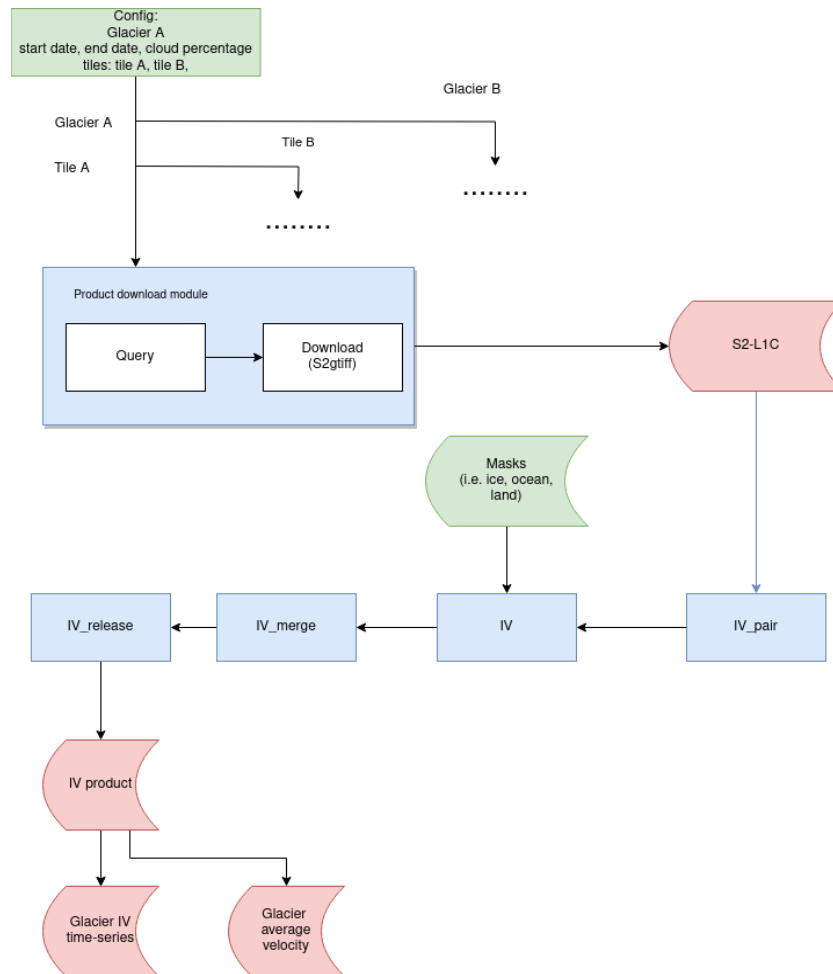


Figure 4.1: Optical IV processing pipeline. Green identifies input data, blue processing modules, white specific processing tasks within a module and red are intermediate and final products. Multiple glaciers can be configured, and for each glacier a subgraph of tiles is generated over which optical IV is measured and finally merged into the final IV release product.

4.3.2.1 Sentinel-2 data query

The first step, named **query** in Figure 4.1, is querying for Sentinel-2 images matching the target date range and the maximum allowed cloud cover. The output is all the Sentinel-2 IDs (S2IDs) matching our target parameters. The processor will then proceed to download the relevant images (all the 10m bands, namely B02, B03, B04 and B08) and convert them to tiff format.

4.3.2.2 Sentinel-2 image pairing

The next step, named **IV_pair** in Figure 4.1, is pairing up S2IDs which are within the date range defined in the configuration. That is, the temporal distance is more than a minimum of e.g., 7 days, and less than a maximum of e.g., 15 days.

4.3.2.3 IV map generation

The IV maps are generated from the S2ID pairs in the step named **IV**, outputting twelve maps for each pair, 3 maps for each band: easting ice velocity, northing ice velocity, and RMS.

Values that are NaN or marked as either ice or water in the provided ice-water mask will not be included in the calculation, as these are assumed to be stationary or missing.

4.3.2.4 IV map merging

The step **IV_merge** takes as input all the generated IV maps, and merges them into a single map. An IV map will only be added if the RMS is below a given threshold. Two types of merge options exist: a temporal weighting with higher emphasis on the values close to the midpoint of the queried time range, and a regular average.

4.3.2.5 IV release product generation

The final step **IV_release** takes the merged IV product, and packages it according to specifications into the deliverable, which is a zipped folder consisting of a short description text, a text containing further comments on the product, a quicklook image, and a NetCDF4 containing the data itself together with relevant metadata.

4.4 Input data and algorithm output

4.4.1 Input data

As with all offset tracing methods, an image pair is required. In the Optical IV pipeline, a pair of Sentinel-2 images are required, of which the band B02 is used. The process of passing image pairs to the IV processor has however been greatly simplified and streamlined by requiring only a select few variables to be specified. These variables are specified in a .yaml-file, and the key variables are the following:

- Start and stop date.
- Maximum allowed cloud coverage for the Sentinel-2 input images.
- Minimum and maximum temporal distance in days between an image pair for the IV map.
- Grid spacing, search chip and reference chip sizes.
- RMS filtering threshold.
- Glacier name and the tile id's associated with the given glacier.

4.4.2 Algorithm output

The output products are the averaged east- and north- ice velocity components and the RMS of the velocity components.

4.5 Accuracy and performance

The feature tracking accuracy is approximately 2 times worse than algorithms based on other types of methods, for example speckle-tracking (De Lange et al., 2007). They are not affected by low or absence of coherence, and they do not have a limit on the maximum measurable velocity magnitude, at least when applied to the range of velocities of the Greenland icesheet (< 13 km/y).

It is also important to highlight that the presence of features in the input imagery is essential for feature tracking. This is often not the case in the interior of the Greenland icesheet. Consequently, this type of algorithm is applied to optical imagery mostly along the margins.

The objective of pre-processing steps is therefore to enhance surface features of the ice, with as little noise, sensor effects, and solar illumination effects as possible. As an example, for having the surface features appear as similar as possible in the sequential imagery, the images should be taken ideally at the same time of day.

The current performance of the processing pipeline allows the processing of a seasonal product for a single glacier to be done within 1 day.

4.6 Capabilities and known limitations

The applicability of offset tracking techniques is limited by the following factors:

- The temporal separation of the image acquisition pairs must be short enough for icesheet features to show little change in their appearance. This temporal separation is glacier and/or season dependent.
- Sun angle variations across the image. These variations reflect in solar illumination effects, which increase the noise in the imagery. A possibility for reducing this noise is to acquire imagery taken at the same time of day. The majority of this should be accounted for by the sun-synchronous orbit of Sentinel-2.
- Cloud coverage. The presence of clouds over ice and/or snow is one of the main sources of noise/failures for offset tracking-based algorithms. A possibility for reducing this noise is to apply a cloud mask before performing offset tracking. While it is impossible to filter out all of the clouds, most of it is filtered out due to having a high RMS.
- The images are already assumed to be co-registered relative to land features. Further, it is assumed that the digital elevation mask (DEM) is reasonably accurate to not give rise to large errors.
- The presence of bed-related topographic features which remain stationary as the ice flows over them may distort the displacements measured.
- The motion of the ice-sheet features should be translational only.

4.7 References

Bernstein, R. (1983), Image geometry and rectification, In Manual of Remote Sensing (R. N. Colwell, ed.), American Society of Photogrammetry, Falls Church, VA, pp.881-884

De Lange, R., A. Luckman, T. Murray Improvement of satellite radar feature tracking for ice velocity derivation by spatial frequency filtering, IEEE Trans. Geosc. Rem. Sens. 45, 2309-2317 (2007).

Derauw, D. DInSAR and Coherence Tracking Applied to Glaciology: The Example of Shirase Glacier, in proc. Fringe'96, (1996).

Gray, A.L., N. Short, K.E. Mattar and K.C. Jezek Velocities and flux of the Filchner ice shelf and its tributaries determined from speckle tracking interferometry, Canadian J. Rem. Sensing 27, 3 (2001).

Joughin, I. Ice-sheet velocity mapping: a combined interferometric and speckle-tracking approach, Annals of Glaciol. 34, 1, 195-201 (2002).

Lucchitta, B.K., C.E. Rosanova & K.F. Mullins Velocities of Pine Island glacier, West Antarctica, from ERS-1 SAR images, Ann. Glaciol. 21, 277-283 (1995).

Michel, R. & E. Rignot Flow of Moreno glacier, Argentina, from repeat-pass Shuttle Imaging Radar images: comparison of the phase correlation method with radar interferometry, J. Glaciol. 45, 149, 93-100 (1999).

Scambos, T. A., Dutkiewicz, M. J., Wilson, J. C., and R. A. Bindschadler (1992): Application of image crosscorrelation to the measurement of glacier velocity using satellite image data. Remote Sensing Environ., 42(3), 177-186.

Fahnestock, M. A., Scambos, T.A., and R. A. Bindschadler (1992): Semi-automated ice velocity determination from satellite imagery. Eos, 73, 493.



5 Gravimetric Mass Balance

5.1 Introduction

The Gravity Recovery and Climate Experiment (GRACE) (Tapley et al., 2004) satellite mission launched in 2002, and terminated its mission in October 2017. The GRACE mission has been highly successful in monitoring the mass loss of the Greenland ice sheet, and provided a clear and unambiguous time series of the mass loss through the GMB ECV (Gravimetric Mass Balance) for the Greenland ice sheet (including outlying glaciers and ice caps), highlighting the dynamic nature of the Greenland ice sheet changes, with record melt in 2012 followed by a decrease in yearly mass loss in the period 2013-17 (Shepherd et al., 2019).

The GRACE data used in the ESA Greenland CCI project, are based on monthly Level-2 gravity fields in spherical harmonics and are available in the period April 2002 through May 2017. As the GRACE mission aged, problems related to accelerometers and batteries in the spacecraft, as well as sunspot conditions, resulted in slightly increasing noise level in the Level 2 data from 2011 onwards. The accelerometer data in the GRACE-B spacecraft was finally turned off in October 2017, and GRACE-A accelerations “transplanted” to GRACE-B, resulting in significantly higher errors in GRACE Level-2 data at the end of the GRACE mission, and therefore also higher errors in the derived mass loss, especially at basin scales.

The GRACE-FO successor mission to GRACE employed a similar K/Ka band microwave tracking link as GRACE, with similar accelerometers to measure non-gravitational accelerations. The GRACE-FO mission (satellite pair GRACE-C and GRACE-D) was launched on May 22, 2018. Unfortunately, the GRACE-D accelerometer in GRACE-FO did not work properly, and GRACE-C data have been transplanted to GRACE-D, similar to the last period of GRACE. Level-2 data from GRACE-FO have been available since June 2018, leaving a 1-year gap in the GMB time series.

Advantages of the GRACE method are that it provides regional averages without the need for interpolation, measures the effect of mass fluctuations directly, and permits monthly temporal sampling. However, a key challenge is to discriminate fluctuations in ice-sheet mass from changes in the underlying crust and mantle. The spatial resolution of GRACE observations derived from global spherical harmonic solutions of about 300 km in the Polar Regions is coarse in comparison to that of other geodetic techniques. Hence, a further complicating factor is that signals may leak into regional GRACE solutions as a consequence of remote geophysical processes.

5.2 Scientific background update

Advantages of the GRACE monitoring of the ice sheets is that it provides regional averages without the need for interpolation, measures the effect of mass fluctuations directly, and permits monthly temporal sampling. However, a key challenge is to discriminate fluctuations in ice-sheet mass from changes in the underlying crust and mantle, especially due to GIA (Glacial Isostatic Adjustment). The disadvantage of GRACE observations is the limited resolution (~300 km) compared to satellite altimetry and ice velocity ECVs. A further complicating factor is that signals may leak into regional GRACE solutions; this is especially a problem in Greenland, where the melt signals of Canadian ice caps, especially in Ellesmere and Devon Islands, cannot be reliably separated from the Greenland melt, without use of auxiliary data, such altimetry-derived mass loss constraints.

For details of the background of the science see the ATBD of the Phase-2 of the CCI project, available at <http://esa-icesheets-cci.org/index.php>, under the link “Phase 2 documents”, and the references in there. Some recent CCI-relevant GRACE papers include Bandikova et al (2019), Bettadpur et al (2018), Forsberg et al (2017), Groh et al (2019, 2021), Döhne et al. (2023), and Shepherd et al (2019). Caron et al (2018) gives a review of GIA models including the recent model to be used in the CCI+ project.

The GRACE and GRACE-FO missions has two identical spacecraft flying about 220 km apart in a polar orbit originally at 500 km above the Earth; the GRACE mission decayed to about 420 km during the mission period, so resolution actually increased during the mission time. The GRACE-FO has been launched to a similar polar orbit as GRACE, with a design lifetime of 5 years; it's hoped that the lifetime will be much longer, as happened with GRACE.

GRACE- and GRACE-FO derived solutions of the Earth's time variable gravity field are available from different official processing facilities (CSR, GFZ and JPL). Level-2 products, provided as spherical harmonic coefficients (Stokes coefficients), are widely used in mass change studies. For the CCI project, independent solutions made at TU Graz was used in Phase-2 of the CCI project (2015-18); due to delays in generating new solutions, the release 6 (R6) of CSR (Center for Space Research, University of Austin) Level-2 products has been used for a parallel solution. The derived CCI products (time-averaged grids) and monthly estimates of the entire ice sheet, as well as 8 drainage basins (Figure 5.1).

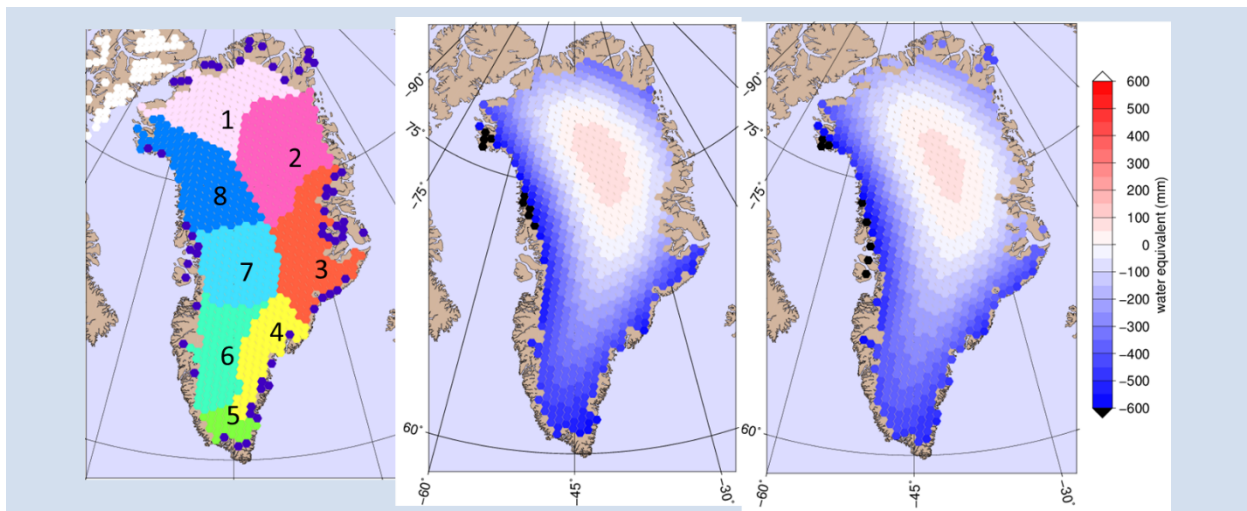


Figure 5.1: Overview of the drainage basin definition and the solution area (left). Blue dots to the left are cells for outlying glaciers and ice caps, some connected to the Greenland ice sheets, some un-connected. Map of trend without including the outer glaciers in the solution area (middle). Map of trend over the whole Greenland, that is including the outer glaciers (right). Due to the limited resolution of GRACE, large “leakage errors” prevent the separation of the ice sheet proper mass loss versus the outlying glaciers. The coast-near mass loss in NW Greenland are similarly impossible to separate from Ellesmere Island eastern ice cap mass losses.

While correlated errors are predominantly affecting the short wavelength (i.e., coefficients of higher spherical harmonic degrees), and shows up in “striping” errors, coefficients of low degrees are also subject to errors. To overcome this limitation C20 is replaced by an estimate derived from SLR observations. Degradation of C30 is mainly related to the use of transplanted accelerometer data. Hence, it is recommended to also replace it with SLR values for all months following August 2016 (Loomis et al., 2020). Gravity fields derived from GRACE data refer to the Earth's center of mass (CM), where the degree-1 term is zero by definition. Therefore degree-1 (C10, C11, S11) estimates based on a combination of GRACE and geophysical model data are used to complement GRACE and the lowest degrees. The replacement values for the degree-1, C20 and C30 terms are given as independent files by the L2 processing centers (TN-13, TN-11, TN-14).

For GRACE-FO, the same processing is applied as for the updated GRACE R6 data from CSR, using the same low-degree terms (recently updated for the whole mission). The data to be released will be based on the available CSR R6 data, and – when available – also the updated ITSG/TU Graz updated L2 data. For more details and references see the Phase 2 ATBD document.

The GRACE and GRACE-FO data apparently shows a good continuation and consistency between missions and is also consistent with long-term CryoSat-derived mass loss trends. Figure 5-2 shows an example of Greenland mass loss from GRACE and GRACE-FO data for the whole ice sheet, using the CCI mascon inversion scheme of DTU Space. An apparent good agreement in trend is seen, and data also highlights the anomalous melt in year 2019, consistent with a usually warm central W Greenland summer, matching the similar 2012 melt event.

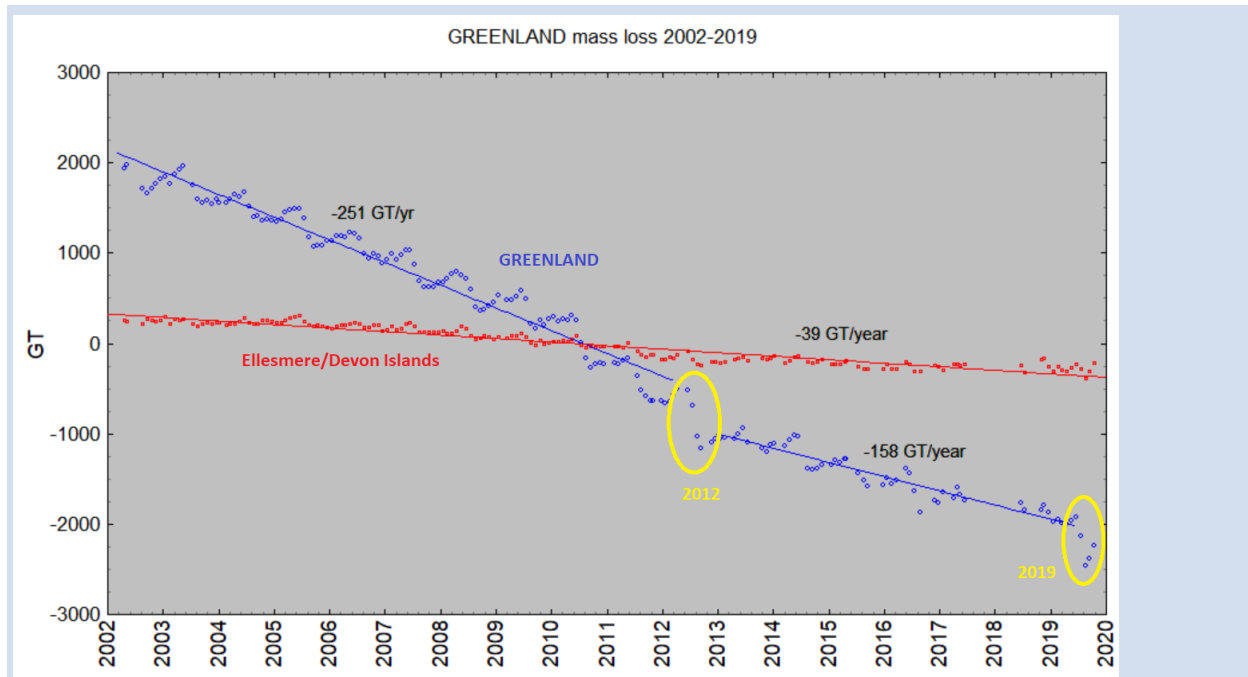


Figure 5.2: Mass loss of the Greenland ice sheet for the combined GRACE and GRACE-FO period (blue), shown along with the estimated mass loss of the Ellesmere Island and Devon Island, Canada, ice caps (red). The apparent continuity of GRACE and GRACE-FO is apparent. The 2012 and 2019 melt events in Greenland is also apparent. The apparent GRACE trends in 2002-2012 and 2013-2019 shows how the Greenland ice sheet melt surprisingly decelerated after the 2012 melt event.

5.3 Algorithms

Methods used for the inference of mass changes from GRACE data is divided into two main groups:

1. Inversion approaches (mascons), as implemented at DTU Space (Barletta et al. 2013, Forsberg et al, 2018)
2. Regional integration approaches, as implemented at TU Dresden (Groh et al, 2019, 2021, Döhne et al., 2023)

The mass inversion method has been adopted for the GMB product generation, primarily in order to be consistent with the ongoing GRACE result release at the national Danish Polarportal (www.polarportal.dk), but also because the mascon inversion approach make it more easy to separate overlapping signals (“leakage”) from adjacent ice caps.

The regional integration approach used in the CCI mass change algorithms, is using tailored sensitivity kernels. These kernels are designed to minimize the sum of GRACE errors, derived from empirical error variance-covariance information, and signal leakage (Groh and Horwath, 2021, Döhne et al. 2023). Details are outlined in the CCI Phase 2 documents.



The methods are applied for GRACE and GRACE-FO in completely the same way as outlined in the CCI Phase 2 ATBD, except for the updated R6 Level 2 data, and the updated long-wavelength spherical harmonic terms for harmonic degrees 1,2 and 3, and the change of the GIA model.

5.4 Input data and algorithm output

Input for the GRACE mascon and regional integration approaches are the same: L2 data from CSR, and later expected L2 products from ITSG, TU Graz). The CSR and ITSG products are based on quite different constraints on the raw L1 GRACE/GRACE-FO data.

Because of the two methodologies used to produce the Greenland mass loss, and the two sets of R2 data, there will eventually be generated four-time GRACE/GRACE-FO time series. The spread of these time series may be used as cross-validation and partially error estimates for the time series. From the Round-Robin exercise carried out in Phase 2 of the CCI project and described in the Round-Robin report of the Phase-2 documents at <http://esa-icesheets-cci.org>. Typical errors estimated in this way are at the 10 GT/year magnitude.

5.5 Capabilities and known limitations

The GRACE time series are at the state-of-the art level, as a.o. confirmed in the recent IMBIE-2 exercise (Shepherd et al., 2019). The main limitation of all GRACE is in the resolution; the source of the mass changes regions of Greenland are known to be associated with a narrow coastal band, as well as with major outlet glacier and ice streams (as evident from the SEC results). Therefore, combined approaches, merging multiple types of data (e.g., both SEC, IV/MFID and GMB) are needed to refine a more detailed GMB product; this is however an area of ongoing research, and the total or basin scale mass loss would likely not change much in such a combined product.

5.6 References

Bandikova T, C McCullough, G Kruizinga, H Save, B Christophe: GRACE accelerometer data transplant. *Advances in Space Research*, Volume 64, Issue 3, 1 August 2019, Pages 623-644, <https://doi.org/10.1016/j.asr.2019.05.021>

Barletta, V. R., Sørensen, L. S., and Forsberg, R. (2013). Scatter of mass changes estimates at basin scale for Greenland and Antarctica. *The Cryosphere*, 7(5), 1411–1432.

Bettadpur, S. (2018). *UTCSR Level-2 Processing Standards Document for Level-2 Product Release 0006*. Austin: Center for Space Research, The University of Texas at Austin.

Caron, L., Ivins, E. R., Larour, E., Adhikari, S., Nilsson, J., & Blewitt, G. (2018). GIA model statistics for GRACE hydrology, cryosphere, and ocean science. *Geophysical Research Letters*, 45, 2203–2212. <https://doi.org/10.1002/2017GL076644>

Döhne, T., Horwath, M., Groh, A., & Buchta, E. (2023). The sensitivity kernel perspective on GRACE mass change estimates. *Journal of Geodesy*, 97(1), 11, <https://doi.org/10.1007/s00190-022-01697-8>

Groh, A., Horwath, M., Horvath, A., Meister, R., Sørensen, L. S., Barletta, V. R., Forsberg, R., Wouters, B., Ditmar, P., Ran, J., Klees, R., Su, X., Shang, K., Guo, J., Shum, C. K., Schrama, E., & Shepherd, A. (2019). Evaluating GRACE Mass Change Time Series for the Antarctic and Greenland Ice Sheet—Methods and Results. *Geosciences*, 9(10), 415.

Groh, A.; Horwath, M. The method of tailored sensitivity kernels for GRACE mass change estimates. In *Proceedings of the EGU General Assembly 2016, Vienna, Austria, 17–22 April 2016; Volume 18*.



Groh, A., M. Horwath (2021): Antarctic Ice Mass Change Products from GRACE/GRACE-FO Using Tailored Sensitivity Kernels. *Remote Sensing*, 13, 1736, <https://doi.org/10.3390/rs13091736>

Forsberg, R., Sørensen, L. & Simonsen, S: Greenland and Antarctica Ice Sheet Mass Changes and Effects on Global Sea Level. *Surveys in Geophysics* (2017) 38: 89. doi:10.1007/s10712-016-9398-7

Kvas, A., Behzadpour, S., Ellmer, M., Klinger, B., Strasser, S., Zehentner, N., & Mayer-Gürr, T. (2019). ITSG-Grace2018: Overview and Evaluation of a New GRACE-Only Gravity Field Time Series. *J. Geophys. Res. Solid Earth*, 124(8), 9332–9344.

Loomis, B. D., Rachlin, K. E., Wiese, D. N., Landerer, F. W., & Luthcke, S. B. (2020). Replacing GRACE/GRACE-FO C30 with satellite laser ranging: Impacts on Antarctic Ice Sheet mass change. *Geophys. Res. Lett.*, . doi:10.1029/2019GL085488.

Shepherd, A, E Ivins, E Rignot, B Smith, M van den Broeke, I Velicogna, P Whitehouse, K Briggs, I Joughin, G Krinner, S Nowicki, T Payne, T Scambos, N Schlegel, A Geruo, C Agosta, A Ahlstrøm, G Babonis, V Barletta, A Bjørk, A Blazquez, J Bonin, W Colgan, B Csatho, R Cullather, M Engdahl, D Felikson, X Fettweis, R Forsberg and the rest of the IMBIE team: Mass balance of the Greenland Ice Sheet from 1992 to 2018. *Nature* (2019) doi:10.1038/s41586-019-1855-2

6 Mass Flow Rate and Ice Discharge

Here we present the mass flow rate and ice discharge (MFID). This work is based on the published data, algorithm, and code from Mankoff et al. (2019) but with the following changes:

- We only use CCI Ice Velocity (IV) data.
- The baseline velocity, used to place the discharge gates, is the average 2016-2018 velocity.
- Surface elevation change is based on CCI Surface elevation change (SEC)
- Gates are 10 km upstream from the baseline termini, rather than 5 km as in Mankoff et al. (2019).
- Cutoff velocity is 150 m yr⁻¹ rather than 100 m yr⁻¹ as Mankoff et al. (2019).

Note that much of the text below is from Mankoff et al. (2019) and is reproduced here either verbatim, or with minor changes to reflect minor changes in the work presented here.

6.1 Introduction

The mass of the Greenland ice sheet is decreasing (e.g., Fettweis et al. (2017), van den Broeke et al. (2017), Wiese et al. (2016), and Khan et al. (2016)). Most ice sheet mass loss – as iceberg discharge, submarine melting, and meltwater runoff – enters the fjords and coastal seas, and therefore ice sheet mass loss directly contributes to sea-level rise (WCRP Global Sea Level Budget Group 2018; Moon et al. 2018; Nerem et al. 2018; Chen et al. 2017). Greenland’s total ice loss can be estimated through a variety of independent methods, for example ‘direct’ mass change estimates from GRACE (Wiese et al. 2016) or by using satellite altimetry to estimate surface elevation change, which is then converted into mass change (using a firn model, e.g. Khan et al. (2016)). However, partitioning the mass loss between ice discharge (D) and surface mass balance (SMB) remains challenging (c.f. Rignot et al. (2008) and Enderlin et al. (2014)). Correctly assessing mass loss, as well as the attribution of this loss (SMB or D) is critical to understanding the process-level response of the Greenland ice sheet to climate change, and thus improving models of future ice-sheet changes and associated sea-level rise (Moon et al. 2018).

6.2 Review of scientific background

The total mass of an ice-sheet, or a drainage basin, changes if the mass gain (SMB inputs, primarily snowfall) is not balanced by the mass loss (D and SMB outputs, the latter generally meltwater runoff). This change is typically termed ice-sheet mass balance (MB) and the formal expression for this rate of change in mass is (e.g., Cuffey and Paterson (2010)),

$$\frac{dM}{dt} = \rho \int_A b dA - \int_g Q dg, \quad (6.1)$$

where ρ is the average density of ice, b is an area mass balance, and Q is the discharge flux. The left-hand side of the equation is the rate of change of mass, the first term on the right-hand side is the area A integrated surface mass balance (SMB), and the second term is the discharge D mass flow rate that drains through gate g . The Equation above is often simplified to

$$MB = SMB - D \quad (6.2)$$

where MB is the mass balance, and referred to as the "input-output" method (e.g. Khan et al. (2015)). Virtually all studies agree on the trend of Greenland mass balance, but large discrepancies persist in both the magnitude and attribution. Magnitude discrepancies include, for example, Kjeldsen et al. (2015) reporting a mass imbalance of -250 ± 21 Gt yr⁻¹ during 2003 to 2010, Ewert, Groh, and Dietrich (2012) reporting -181 ± 28 Gt yr⁻¹ during 2003 to 2008, and Rignot et al. (2008) reporting a mass imbalance of -265 ± 19 Gt yr⁻¹

during 2004 to 2008. Some of these differences may be due to different ice sheet area masks used in the studies. Attribution discrepancies include, for example, Enderlin et al. (2014) attributing the majority (64 %) of mass loss to changes in SMB during the 2005 to 2009 period but Rignot et al. (2008) attributing the majority (85 %) of mass loss to changes in D during the 2004 to 2008 period.

Discharge may be calculated through several methods, including mass flow rate through gates (e.g., Enderlin et al. (2014), King et al. (2018), and J. Mouginot et al. (2019)), or solving as a residual from independent mass balance terms (e.g. Kjær et al. (2012; Kjeldsen et al. 2015)). The gate method that we use in this study incorporates ice thickness and an estimated vertical profile from the observed surface velocity to calculate the discharge. A typical formulation of discharge across a gate D_g is,

$$D_g = \rho V H w, \quad (6.3)$$

where ρ is the average density of ice, V is depth-average gate-perpendicular velocity, H is the ice thickness, and w is the gate width. Uncertainties in V and H naturally influence the estimated discharge. At fast-flowing outlet glaciers, V is typically assumed to be equal at all ice depths, and observed surface velocities can be directly translated into depth-averaged velocities (as in Enderlin et al. (2014), and King et al. (2018)). To minimise uncertainty from SMB or basal mass balance corrections downstream of a flux gate, the gate should be at the grounding line of the outlet glacier. Unfortunately, uncertainty in bed elevation (translating to ice thickness uncertainty) increases toward the grounding line. To minimise downstream SMB effects, we put gates as close as possible to the grounding line.

6.3 Algorithms

6.3.1 Terminology

We use the following terminology:

- "Pixels" are individual 200 m x 200 m raster discharge grid cells. We use the nearest neighbour when combining data sets that have different grid properties.
- "Gates" are contiguous (including diagonal) clusters of pixels.
- "Sectors" are spatial areas that have 0, 1, or > 1 gate(s) plus any upstream source of ice that flows through the gate(s), and come from Zwally et al. (2012).
- The "baseline" period is the average 2016-2018 velocity from available CCI IV winter mosaics.
- "Fast-flowing ice" is defined as ice that flows more than 150 m yr⁻¹.
- Names are reported using the official Greenlandic names from Bjørk, Kruse, and Michaelsen (2015) if a nearby name exists, then Mouginot and Rignot (2019) in parentheses.

Although we refer to solid ice discharge, and it is in the solid phase when it passes the gates and eventually reaches the termini, submarine melting does occur at the termini and some of the discharge enters the fjord as liquid water (Enderlin and Howat 2013).

6.3.2 Gate Location

We use the following terminology:

Gates are algorithmically generated for fast-flowing ice (greater than 150 m yr⁻¹) close to the ice sheet terminus determined by the baseline-period data. We apply a 2D inclusive mask to the baseline data for all



ice flowing faster than 150 m yr^{-1} . We then select the mask edge where it is near the BedMachine ice mask (not including ice shelves), which effectively provides grounding line termini. We buffer the termini 10 km in all directions creating ovals around the termini and once again down-select to fast-flowing ice pixels. This procedure results in gates 10 km upstream from the baseline terminus that bisect the baseline fast-flowing ice. We manually mask some land- or lake-terminating glaciers which are initially selected by the algorithm due to fast flow and mask issues.

We select a 150 m yr^{-1} speed cut-off because slower ice, taking longer to reach the terminus, is more influenced by SMB. The choice of a 10 km buffer follows from the fact that it is near-terminus and thus avoids the need for (minor) SMB corrections downstream, yet is not too close to the terminus where discharge results are sensitive to the choice of distance-to-terminus value (Mankoff et al. 2019), which may be indicative of bed (ice thickness) errors.

6.3.3 Thickness

We derive thickness from the BedMachine surface and bed elevation. We adjust the surface through time by linearly interpolating the SEC product and adding it to the BedMachine surface. Finally, from the fixed bed and temporally varying surface, we calculate the time-dependent ice thickness at each gate pixel.

6.3.4 Missing or invalid data

The baseline data provides velocity at all gate locations by definition, but individual non-baseline velocity maps often have missing or invalid data. Also, thickness provided by BedMachine is clearly incorrect in some places (e.g. fast-flowing ice that is 10 m thick, Figure 6-1). We define invalid data and fill in missing data as described below.

1. Missing IV

We generate an ice speed time series by assigning the IV product to the middle of their reported time span. Velocities are sampled only where there are gate pixels. Missing pixel velocities are linearly interpolated in time, except for missing data at the beginning of the time series which are back- and forward-filled with the temporally-nearest value for that pixel.

2. Missing SEC

Where SEC is missing, we use the provided BedMachine ice thickness.

3. Invalid thickness

The thickness data appear to be incorrect in some locations. For example, many locations have fast-flowing ice, but report ice thickness as 10 m or less. We accept all ice thickness greater than 20 m and construct from this a thickness versus \log_{10} speed relationship. For all ice thickness less than or equal to 20 m thick we adjust thickness based on this relationship. We selected the 20 m thickness cut-off after visually inspecting the velocity distribution. This thickness adjustment adds 20 Gt yr^{-1} to our baseline-period discharge estimate with no adjustment.

6.3.5 Discharge

We calculate discharge per pixel using density (917 kg m^{-3}), Filled ice velocity, projection-corrected pixel width, and adjusted ice thickness derived from time-varying surface elevation and a fixed bed elevation. We

assume that any change in surface elevation corresponds to a change in ice thickness and thereby neglect basal uplift, erosion, and melt, which combined are orders of magnitude less than surface melting (e.g., Cowton et al. (2012), Khan et al. (2007)). We also assume depth-averaged ice velocity is equal to the surface velocity.

We calculate discharge using the gate-orthogonal velocity at each pixel and at each timestamp – all velocity estimates are gate-orthogonal at all times, regardless of gate position, orientation, or changing glacier velocity direction over time.

6.4 Input data and algorithm output

6.4.1 Input Data

The discharge gates in this study are generated using only surface speed and an ice mask. We use CCI ice velocity (IV) and the BedMachine v5 (M. Morlighem, Williams, et al. 2017a, 2022) ice mask, and BedMachine for initial ice thickness, supplemented with the SEC product from this project. Official glacier names come from Bjørk, Kruse, and Michaelsen (2015). Other glacier names come from Mouginot and Rignot (2019).

Table 6.1: Summary of data sources used in this work.

Property	Name used in this paper	Reference
Basal Topography	BedMachine	M. Morlighem, Williams, et al. (2017a, 2022)
Surface Elevation	BedMachine	M. Morlighem, Williams, et al. (2017a, 2022)
Surface Elevation Change	Surface Elevation Change	CCI+ SEC
Baseline Velocity	Baseline	CCI+ IV 2016-2018 average
Velocity	CCI IV	CCI+ IV
Sectors & Regions	Sectors & Regions	Mouginot and Rignot (2019)
Names		Bjørk, Kruse, and Michaelsen (2015; Mouginot and Rignot 2019)

6.4.2 Algorithm Output

The output of the algorithm is a set of CSV files with time (quarterly) and discharge (by region from Zwally et al. (2012)).

6.5 Accuracy and performance

6.5.1 Accuracy

The algorithm and data product introduced here are closely related to the algorithm and data product introduced by Mankoff et al. (2019). When comparing annual average over all of Greenland, then this product and the product released by Mankoff et al. (2019) agree well. Comparing by regions is difficult because this product is binned on the Zwally et al. (2012) and Mankoff et al. (2019) is on the Mouginot and Rignot (2019) regions and sectors. Comparing by regions is difficult because this product is binned on the Zwally et al. (2012) and Mankoff et al. (2019) is on the Mouginot and Rignot (2019) regions and sectors.

Table 6.2: Comparison between this product ("this") and Mankoff et al. (2019) ("m2019")

Date	this	this _{err}	m2019	m2019 _{err}	Diff	diff %
------	------	---------------------	-------	----------------------	------	--------



2014-10-31	458.201	41.714	493.947	50.835	-35.746	-7.80
2014-11-30	458.064	41.684	499.001	51.361	-40.937	-8.93
2014-12-31	458.933	41.739	499.686	51.421	-40.753	-8.87
2015-01-31	459.531	41.785	498.548	51.119	-39.016	-8.49
2015-02-28	458.165	41.595	498.392	50.959	-40.226	-8.77
2015-03-31	464.214	42.119	500.767	51.545	-36.553	-7.87
2015-04-30	471.51	42.758	0	0	471.51	100
2015-05-31	481.213	43.613	498.79	51.057	-17.577	-3.65
2015-06-30	484.541	43.863	0	0	484.541	100
2015-07-31	476.351	42.776	515.999	52.900	-39.648	-8.32
2015-08-31	466.619	42.14	498.024	50.989	-31.405	-6.73
2015-09-30	463.94	41.987	500.495	51.367	-36.555	-7.87
2015-10-31	460.43	41.725	498.883	51.175	-38.453	-8.35
2015-11-30	464.914	42.103	0	0	464.914	100
2015-12-31	459.72	41.69	499.037	51.197	-39.317	-8.55
2016-01-31	458.423	41.547	493.502	50.658	-35.07	-7.65
2016-02-29	457.078	41.436	0	0	457.07	100
2016-03-31	456.667	41.487	492.947	50.691	-36.28	-7.94
2016-04-30	470.318	42.652	0	0	470.31	100
2016-05-31	476.316	43.147	498.546	51.527	-22.23	-4.66
2016-06-30	482.292	43.864	0	0	482.29	100
2016-07-31	484.153	43.746	504.007	51.724	-19.854	-4.10
2016-08-31	468.55	42.54	493.635	50.693	-25.085	-5.35
2016-09-30	463.512	42.22	495.268	50.779	-31.756	-6.85
2016-10-31	476.721	43.55	495.857	50.883	-19.136	-4.01
2016-11-30	477.397	43.765	497.649	50.985	-20.251	-4.24
2016-12-31	477.492	43.789	497.671	50.958	-20.178	-4.22
2017-01-31	467.408	43.152	500.478	51.104	-33.069	-7.07
2017-02-28	469.127	43.734	500.683	51.156	-31.555	-6.72
2017-03-31	475.137	44.192	500.946	51.152	-25.809	-5.43
2017-04-30	480.697	44.753	507.796	52.366	-27.099	-5.63
2017-05-31	497.159	46.091	508.157	52.198	-10.997	-2.21
2017-06-30	499.296	46.247	507.599	51.486	-8.303	-1.66
2017-07-31	511.125	47.02	516.857	52.238	-5.732	-1.12
2017-08-31	495.171	45.175	507.64	51.063	-12.468	-2.51
2017-09-30	485.009	44.618	503.394	50.932	-18.385	-3.79
2017-10-31	486.657	44.754	506.185	51.447	-19.527	-4.01
2017-11-30	486.16	44.813	500.558	50.628	-14.398	-2.96
2017-12-31	483.653	44.649	501.124	50.796	-17.470	-3.61
2018-01-31	475.525	43.983	501.139	51.101	-25.614	-5.38

2018-02-28	475.491	43.971	499.779	50.901	-24.287	-5.10
2018-03-31	479.596	44.512	497.692	50.549	-18.096	-3.77
2018-04-30	481.411	44.726	495.004	50.165	-13.592	-2.82
2018-05-31	490.03	45.563	501.054	51.082	-11.024	-2.24
2018-06-30	498.167	46.298	496.822	50.772	1.345	0.26
2018-07-31	501.924	46.577	500.902	50.922	1.021	0.20
2018-08-31	491.054	44.961	497.571	50.385	-6.517	-1.32
2018-09-30	480.914	44.18	487.941	49.487	-7.027	-1.46
2018-10-31	480.203	44.399	499.935	51.104	-19.732	-4.10
2018-11-30	482.441	44.774	498.129	50.659	-15.688	-3.25
2018-12-31	478.485	44.463	496.089	50.685	-17.604	-3.67
2019-01-31	477.047	44.43	498.34	51.198	-21.293	-4.46
2019-02-28	481.548	44.936	497.903	51.034	-16.354	-3.39
2019-03-31	482.447	45.126	495.642	50.532	-13.195	-2.73
2019-04-30	491.115	45.852	499.428	51.132	-8.313	-1.69
2019-05-31	497.503	46.409	502.146	51.749	-4.643	-0.93
2019-06-30	513.127	48.037	507.756	52.096	5.370	1.04
2019-07-31	505.819	46.779	505.35	51.441	0.469	0.09

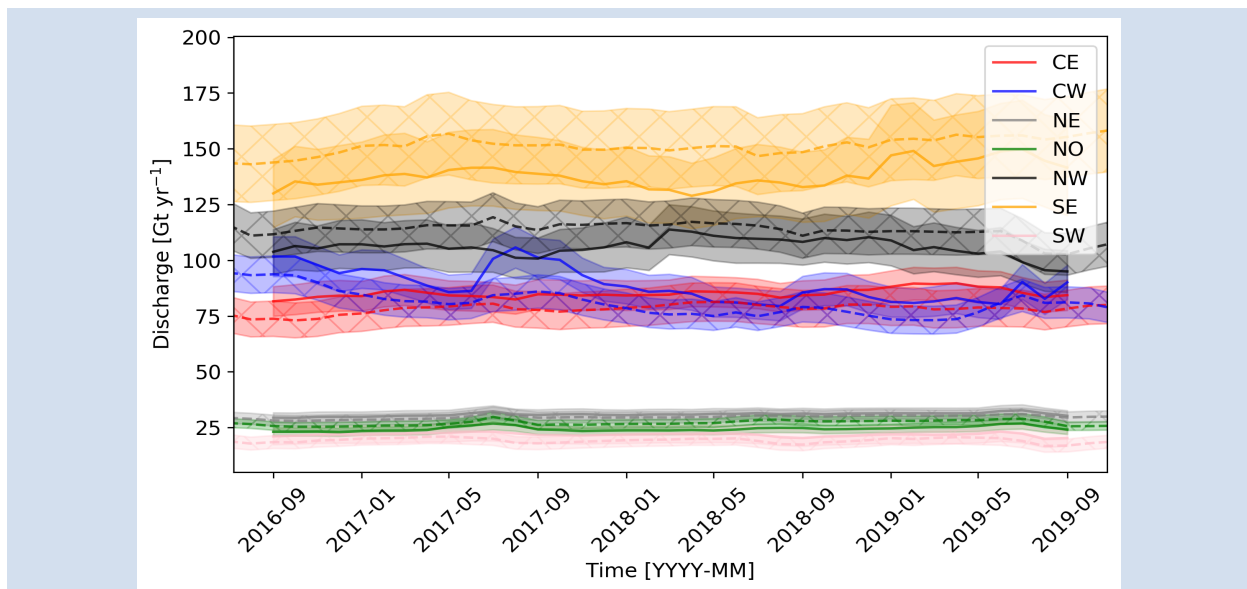


Figure 6.1: Comparison between this and Mankoff et al. (2019) monthly discharge by region. Solid line is this product, and solid fill is this product uncertainty. Dashed line and hatch fill are Mankoff et al. (2019).

6.5.2 Performance

The code takes ~ 1 hour to run after the input data products have been downloaded and placed in the necessary location. Downloading input data and installing all required software is not automated, but once those dependencies are met, the algorithm is publicly available. Repeated runs make some use of the static computational results of earlier runs and take less time to calculate discharge for updated velocity products. If SEC change or thickness products change, a full re-run is required.



6.6 Capabilities and known limitations

We note the following major limitations to the current implementation.

- Discharge is only calculated where gates are placed. This means discharge less than the cut-off velocity is not considered, and that if a glacier does not currently have a gate surges in the future, that surge will not be captured in the discharge unless the gates are recalculated.
- We use relatively raw products as provided from 3rd parties. We do not apply smoothing filters to the velocity product, and only adjust the thickness product where it is clearly incorrect (fast-flowing ice < 20 m thick).

6.7 References

- Bjørk, A. A., L. M. Kruse, and P. B. Michaelsen. 2015. "Brief Communication: Getting Greenland's Glaciers Right – a New Dataset of All Official Greenlandic Glacier Names." *The Cryosphere* 9 (6): 2215–8. <https://doi.org/10.5194/tc-9-2215-2015>.
- Chen, Xianyao, Xuebin Zhang, John A. Church, Christopher S. Watson, Matt A. King, Didier Monselesan, Benoit Legresy, and Christopher Harig. 2017. "The Increasing Rate of Global Mean Sea-Level Rise During 1993–2014." *Nature Climate Change* 7 (7): 492–95. <https://doi.org/10.1038/nclimate3325>.
- Cowton, T., Peter Nienow, Ian D. Bartholomew, A. Sole, and Douglas W. F. Mair. 2012. "Rapid Erosion Beneath the Greenland Ice Sheet." *Geology* 40: 343–46. <https://doi.org/10.1130/G32687.1>.
- Cuffey, Kurt M., and W. S. B. Paterson. 2010. *The Physics of Glaciers*. Fourth. Academic Press.
- Enderlin, Ellyn M., and Ian M. Howat. 2013. "Submarine Melt Rate Estimates for Floating Termini of Greenland Outlet Glaciers (2000 – 2010)." *Journal of Glaciology* 59 (213): 67–75. <https://doi.org/10.3189/2013JoG12J049>.
- Enderlin, Ellyn M., Ian M. Howat, Seongsu Jeong, Myoung-Jong Noh, Jan H. van Angelen, and Michiel R. van den Broeke. 2014. "An Improved Mass Budget for the Greenland Ice Sheet." *Geophysical Research Letters* 41 (3): 866–72. <https://doi.org/10.1002/2013GL059010>.
- Ewert, H., A. Groh, and R. Dietrich. 2012. "Volume and Mass Changes of the Greenland Ice Sheet Inferred from ICESat and GRACE." *Journal of Geodynamics* 59-60 (September): 111–23. <https://doi.org/10.1016/j.jog.2011.06.003>.
- Fettweis, Xavier, Jason E. Box, Cécile Agosta, Charles Amory, Christoph Kittel, Charlotte Lang, Dirk Van As, Horst Machguth, and Hubert Gallée. 2017. "Reconstructions of the 1900–2015 Greenland Ice Sheet Surface Mass Balance Using the Regional Climate MAR Model." *The Cryosphere* 11 (2): 1015–33. <https://doi.org/10.5194/tc-11-1015-2017>.
- Khan, S. A., I. Sasgen, M. Bevis, T. van Dam, J. L. Bamber, J. Wahr, M. Willis, et al. 2016. "Geodetic Measurements Reveal Similarities Between Post-Last Glacial Maximum and Present-Day Mass Loss from the Greenland Ice Sheet." *Science Advances* 2 (9): e1600931–e1600931. <https://doi.org/10.1126/sciadv.1600931>.
- Khan, Shfaqat A, Andy Aschwanden, Anders A Bjørk, John Wahr, Kristian K Kjeldsen, and Kurt H Kjær. 2015. "Greenland Ice Sheet Mass Balance: A Review." *Reports on Progress in Physics* 78 (4): 046801. <https://doi.org/10.1088/0034-4885/78/4/046801>.
- Khan, Shfaqat A., John Wahr, Leigh A. Stearns, Gordon S. Hamilton, Tonie van Dam, Kristine M. Larson, and Olivier Francis. 2007. "Elastic Uplift in Southeast Greenland Due to Rapid Ice Mass Loss." *Geophysical Research Letters* 34 (21). <https://doi.org/10.1029/2007gl031468>.



Khvorostovsky, Kirill S. 2012. "Merging and Analysis of Elevation Time Series over Greenland Ice Sheet from Satellite Radar Altimetry." *IEEE Transactions on Geoscience and Remote Sensing* 50 (1): 23–36. <https://doi.org/10.1109/tgrs.2011.2160071>.

King, Michalea D., Ian M. Howat, Seongsu Jeong, Myoung J. Noh, Bert Wouters, Brice Noël, and Michiel R. van den Broeke. 2018. "Seasonal to Decadal Variability in Ice Discharge from the Greenland Ice Sheet." *The Cryosphere* 12 (12): 3813–25. <https://doi.org/10.5194/tc-12-3813-2018>.

Kjeldsen, Kristian K., Niels J. Korsgaard, Anders A. Bjørk, Shfaqat A. Khan, Jason E. Box, Svend Funder, Nicolaj K. Larsen, et al. 2015. "Spatial and Temporal Distribution of Mass Loss from the Greenland Ice Sheet Since AD 1900." *Nature* 528 (7582): 396–400. <https://doi.org/10.1038/nature16183>.

Kjær, Kurt H., Shfaqat A. Khan, Niels J. Korsgaard, John Wahr, Jonathan L. Bamber, Ruud Hurkmans, Michiel R. Van Den Broeke, et al. 2012. "Aerial Photographs Reveal Late-20th-Century Dynamic Ice Loss in Northwestern Greenland." *Science* 337 (6094): 569–73. <https://doi.org/10.1126/science.1220614>.

Mankoff, Kenneth D., William Colgan, Anne Solgaard, Nanna B. Karlsson, Andreas P. Ahlstrøm, Dirk van As, Jason E. Box, et al. 2019. "Greenland Ice Sheet Solid Ice Discharge from 1986 Through 2017." *Earth System Science Data* 11 (2): 769–86. <https://doi.org/10.5194/essd-11-769-2019>.

Moon, Twila, Andreas Ahlstrøm, Heiko Goelzer, William Lipscomb, and Sophie Nowicki. 2018. "Rising Oceans Guaranteed: Arctic Land Ice Loss and Sea Level Rise." *Current Climate Change Reports*, July. <https://doi.org/10.1007/s40641-018-0107-0>.

Morlighem, M., C. N. Williams, E. Rignot, L. An, J. E. Arndt, J. L. Bamber, G. Catania, et al. 2017a. "BedMachine V3: Complete Bed Topography and Ocean Bathymetry Mapping of Greenland from Multi-Beam Echo Sounding Combined with Mass Conservation." *Geophysical Research Letters*, September. <https://doi.org/10.1002/2017gl074954>.

Morlighem, M., C. Williams, E. Rignot, L. An, J. E. Arndt, J. Bamber, G. Catania, et al. 2022. "IceBridge BedMachine Greenland, Version 5. Boulder, Colorado USA. NASA National Snow and Ice Data Center Distributed Active Archive Center. <https://doi.org/10.5067/GMEVBWFLWA7X>.

Mouginot, Jeremie, and Eric Rignot. 2019. "Glacier Catchments/Basins for the Greenland Ice Sheet." UC Irvine. <https://doi.org/10.7280/d1wt11>.

Mouginot, Jérémie, Eric Rignot, Anders A. Bjørk, Michiel van den Broeke, Romain Millan, Mathieu Morlighem, Brice Noël, Bernd Scheuchl, and Michael Wood. 2019. "Forty-Six Years of Greenland Ice Sheet Mass Balance from 1972 to 2018." *Proceedings of the National Academy of Sciences*, April, 201904242. <https://doi.org/10.1073/pnas.1904242116>.

Nerem, R. S., B. D. Beckley, J. T. Fasullo, B. D. Hamlington, D. Masters, and G. T. Mitchum. 2018. "Climate-Change–Driven Accelerated Sea-Level Rise Detected in the Altimeter Era." *Proceedings of the National Academy of Sciences* 115 (9): 2022–5. <https://doi.org/10.1073/pnas.1717312115>.

Rignot, Eric J., Jason E. Box, Evan W. Burgess, and Edward Hanna. 2008. "Mass Balance of the Greenland Ice Sheet from 1958 to 2007." *Geophysical Research Letters* 35 (L20502). <https://doi.org/10.1029/2008GL035417>.

Simonsen, Sebastian B., and Louise Sandberg Sørensen. 2017. "Implications of Changing Scattering Properties on Greenland Ice Sheet Volume Change from Cryosat-2 Altimetry." *Remote Sensing of Environment* 190 (March): 207–16. <https://doi.org/10.1016/j.rse.2016.12.012>.

Sørensen, Louise Sandberg, Sebastian B. Simonsen, Rakia Meister, René Forsberg, Joanna F. Levinsen, and Thomas Flament. 2015. "Envisat-Derived Elevation Changes of the Greenland Ice Sheet, and a Comparison



with ICESat Results in the Accumulation Area.” *Remote Sensing of Environment* 160 (April): 56–62. <https://doi.org/10.1016/j.rse.2014.12.022>.

Sørensen, S., S. Simonsen, R. Meister, R. Forsberg, and K. Khvorostovsky. 2015. “Surface Elevation Changes of the Greenland Ice Sheet from Satellite Radar Altimetry.”

van den Broeke, Michiel, Jason Box, Xavier Fettweis, Edward Hanna, Brice Noël, Marco Tedesco, Dirk Van As, Willem Jan Van De Berg, and Leo Van Kampenhout. 2017. “Greenland Ice Sheet Surface Mass Loss: Recent Developments in Observation and Modeling.” *Current Climate Change Reports*, November. <https://doi.org/10.1007/s40641-017-0084-8>.

WCRP Global Sea Level Budget Group. 2018. “Global Sea-Level Budget 1993 Present.” *Earth System Science Data* 10 (3): 1551–90. <https://doi.org/10.5194/essd-10-1551-2018>.

Wiese, D. N., D.-N. Yuan, C. Boening, F. W. Landerer, and M. M. Watkins. 2016. “JPL GRACE Mascon Ocean, Ice, and Hydrology Equivalent HDR Water Height RL05M.1 CRI Filtered Version 2.” PO.DAAC, CA, USA. <https://doi.org/10.5067/TEMSC-2LCR5>.

Zwally, H. Jay, M. Giovinetto, M. A. Beckley, and Jack L. Saba. 2012. “Antarctic and Greenland Drainage Systems.” http://icesat4.gsfc.nasa.gov/cryo_data/ant_grn_drainage_systems.php.



7 Supraglacial Lakes (SGL)

7.1 Introduction

This section gives an overview of the identification of supraglacial lakes (SGLs) on the Greenland Ice sheet using deep learning (DL) models applied to Sentinel-2 imagery, and ICESat-2 derived depth measures. We developed and trained a model able to estimate both lake extent and depth from S2 images. Should this S2-based model prove good enough it can allow a much higher update rate of SGL over the Greenland Ice Sheet (GrIS), this is based on comparing S2 revisit rates of 3-6 days to the 92 day revisit rate of ICESat-2. Ultimately this can provide a higher time-resolution for tracking the appearance, and subsequent disappearance of SGLs.

7.2 Review of scientific background

Mapping of supraglacial lakes has earlier been done using standard indices to enhance the spectral signature of water, e.g the NDWI index. These spectral signatures are affected by several factors, which has been addressed in earlier iterations. Earlier methods were adapted from Yang and Smith (2013). In this iteration we are looking at using DL methods which have been deemed feasible for the application. We base our method on a U-Net architecture (Ronneberger, et al. 2015), which has become one of the most common architectures for segmentation tasks in remote sensing data.

The lake depth estimates are generated by DTU Space using the “Watta” algorithm (Datta, R.T. & Wouters, B. 2021). Watta is a synthesis of earlier knowledge and principles described in Parrish, C.E. et al. 2019, Fair, Z. et al 2020, and Fricker, H.A. et al 2021. The algorithm computes a series of probability ratio considerations to form an adaptive decision tree. These corrections and refinements converge to yield altitude points corresponding to the lake surface and a lake bottom. These can then be interpolated so as to form a line of depth estimates. The quality of the estimates depend on water clarity, as well as the underlying lake geometry, where only the latter can be accounted for within the scope of the implemented model.

The U-Net architecture for convolutional neural networks was first used for segmentation of medical imagery in 2015, and has in recent years been successfully applied to remote sensing data over the GrIS as well as other areas (e.g. Jiang D, et. al. 2022, Hou Y, et al. 2021). In earlier experiments with this architecture our results showed that we can successfully adapt U-Nets to the dual task of lake extent and depth, and the continuation of this is likely to provide a model that is sufficiently robust.

7.3 Algorithms

We are basing our neural network on a U-Net architecture, which is also able to give a secondary prediction of depth in addition to the segmentation of lake vs no-lake 2D mask. We use an implementation in PyTorch with an internally developed interface for managing the complexities of the geospatial data pipelines. Sampling the data is done in a weighted manner, so as to ensure a fair representation of samples with and without lakes present. Masking of the lakes are from an earlier GIS CCI data product (SGL, developed by ASIAQ), where shapes of SGLs for the melt-season of 2019 are provided.

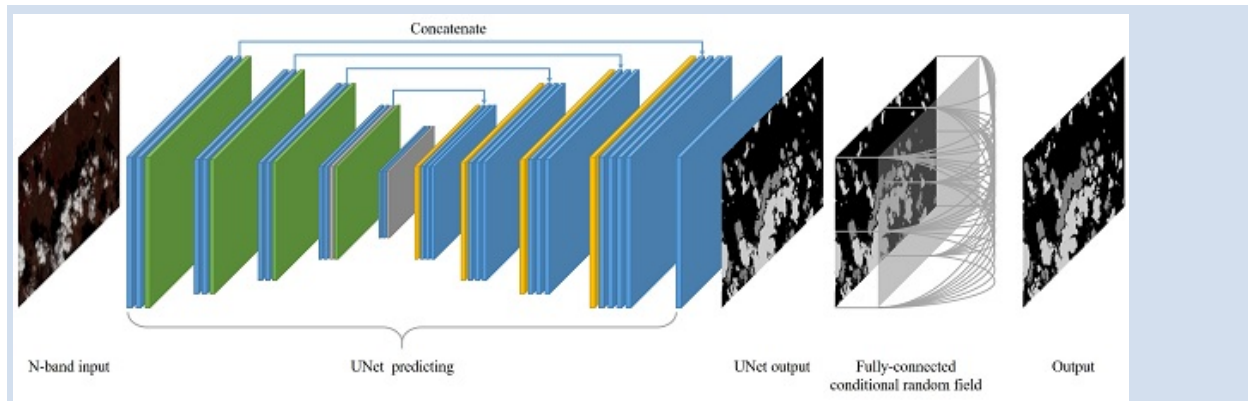


Figure 7.1: Example U-net architecture with conditional random field (CRF) figure from Jiao L, et. al. (2020)

The input data is Sentinel-2 imagery.

Training the neural network is handled on local servers. It is an application of gradient descent, using the AdamW optimizer. Hyperparameter tuning will be a larger factor towards the end of the project, where we will tune the best possible model from the families of experiments performed. Similar optimizations to increase performance with ensembling techniques et.c. will also be performed.

In data processing there are multiple interesting avenues to explore. These include Unsupervised Data Augmentations for Consistency-training (Xie, Q. 2019), wherein one allows the models to learn from unlabelled data that is of a sufficiently high confidence under advanced augmentations. (i.e. If the model remains certain about the predictions after rotating the image then it is said to be consistent, in which case it can backpropagate on unlabelled data with demonstrable benefits to performance.) Similarly, we perform experiments using pseudo-labelling, and strategic unlabelling of low-consistency data. Pseudo-labels are labels generated by the model, where these prove consistent, and is an established method for semi-supervised learning. We also make use of pseudo-unlabelling, where samples that prove in strong, repeated disagreement with the model predictions are unlabelled - i.e. designated as unlabelled data. This has also proven to be a useful indicator of likely mislabels, and in combination with mixing techniques can allow the model to perform dynamic relabelling without loss of performance.

Further there is the consideration of loss-functions, where we test different combinations of the regression-loss vs the segmentation-loss, as part of the hyperparameter tuning. For the segmentation task we employ a Focal loss (ref), which acts as a weighted variation of the cross-entropy, giving higher preference towards learning the more difficult target labels. The focal loss has tunable parameters which will be explored in the hyperparameter tuning phase.

Regarding the data test-split, we perform a cut and assign the data into three classes: training, validation, and test. The test-data is the unseen data that is not part of the decision making process, and is used for unbiased reporting of how the model performs in a realistic setting (It is therefore recommended that one ensures this set is representative of both the real world where the model will be deployed, as well as the training and validation sets respectively).

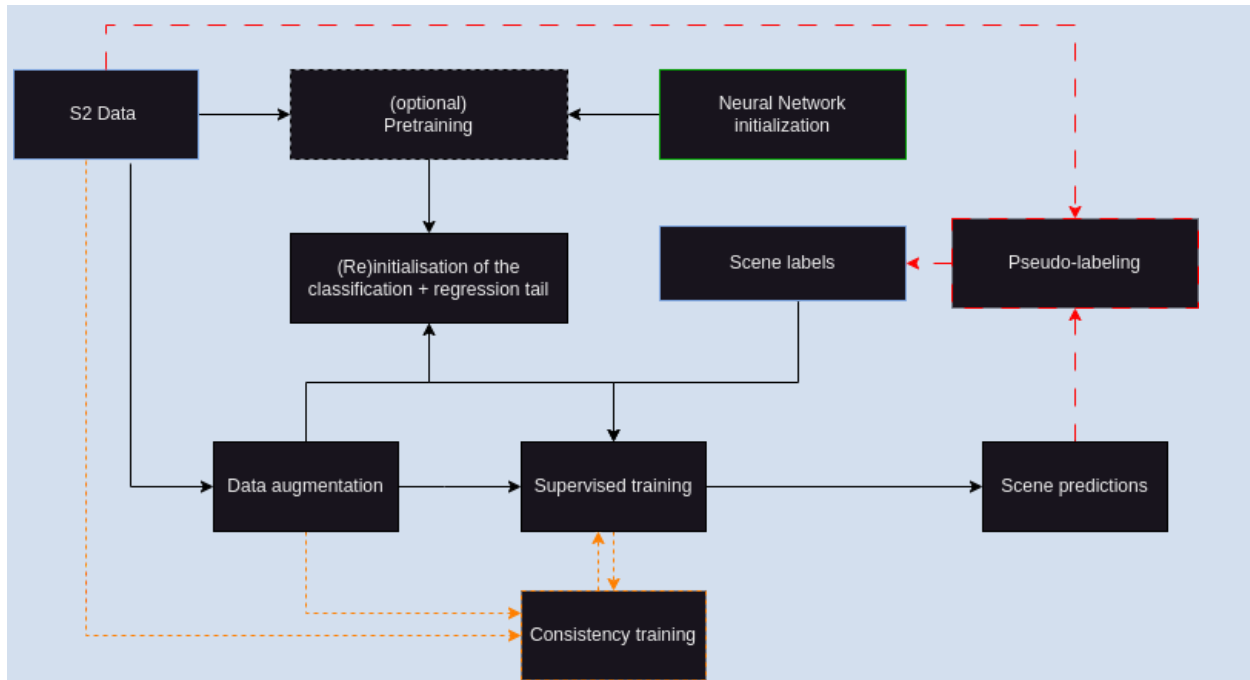


Figure 7.2: Initialization and data/processing pipeline.

The pipeline is presented in Figure 7.2 and it is composed by the following steps:

1. Initialisation of a network with either:
 - a. Random weights.
 - b. Weights from pre-trained network (optional).
2. Central training loop:
 - a. Feed input data to the network.
 - b. Calculate the error w.r.t. the ground truth, using the loss functions.
 - c. Backpropagate and update the weights.
 - d. Repeat for N epochs.
3. Consistency-training:
 - a. Any unlabelled data is sampled and fed through the model to generate predictions.
 - b. The same data is also augmented/transformed, and then used to generate predictions.
 - c. These two previous predictions are compared. If these are in agreement then the prediction is assumed to be correct, and the model will learn from it.
4. Pseudo-labelling:
 - a. Pseudo labels will be considered for use, where these can be validated.
5. As the model is trained, the best performance is calculated over the validation set.
6. If doing hyperparameter search, then the model is also compared to variations of itself with different hyperparameter settings.
7. The best performing model on the validation set is then measured against the test-set, and reported as a final performance value of that model class.

Pre-training the network can be done in different ways, of which the most available are to pre-train by sorting the training data by date (Cong, Y 2022), seasonal contrast (Mañas, O.,2021), or by pre-training on ImageNet (Wang, D., 2022). This loop is performed for all the different classes of models we wish to explore, along with the variations over hyperparameters for each class of models.

For a deployment model it is also common to perform a further training where the validation- and test-sets are included in the final training. This would ensure that the delivery model is fully tuned on all the available



data. During the finalisation of our model, we will therefore perform a final training to ensure the model is as optimised as far as we can with the available data.

7.4 Input data and algorithm output

The input data is Sentinel 2A and 2B scenes (L2A) during the summer melt season. No distinction is made between ascending and descending scenes.

The output data is rasterized masks which demarcate the lake extent, and associated pixel values within these that correspond to a maximum likelihood depth. Further the output will be post-processed, removing artefacts and other forms of noise that are likely to appear.

7.5 Performance Measures

For measuring the lake extent, we will use the (macro-averaged) F1 measure, which is a common measure capturing the performance of segmentation tasks. For the regression task we employ a mean absolute error.

7.6 Capabilities and known limitations

The use of U-Net neural networks seems a robust method for semantic segmentation in general, and it has successfully been used for SGL extent, e.g. Jiang D et. al. (2022). These give a rasterized output, where each pixel in an input image has a corresponding output pixel which is classified based on maximum likelihood. This means that the model is sensitive to outliers, which is common across most neural networks, and there can be occasional mislabelled pixels. Such mislabels will be dealt with using post-processing.

Concerning the regression task of estimating lake depth, the lack of data presents as the main problem. Since we rely on narrow tracks across the ice as source data for the depth-estimates, these are naturally sparse. The margins of error also increase with deeper lakes. As such we will need to preprocess the data before training our model to weigh the data based on depth.

The combination of these two outputs from a single model can enhance the performance of either task, but it also requires more care be put into balancing the two. Generally the limitations revolve around the amount of data, as well as the quality of data. Amelioration of this issue can be done by manual verification of the data, which is a time-consuming process. Similarly we also see that the algorithm may struggle with rocks, and debris in the vicinity of the lakes, as well as crevasses or ice-covered lakes.

7.7 References

Datta, R. T. & Wouters, B. Supraglacial lake bathymetry automatically derived from ICESat-2 constraining lake depth estimates from multi-source satellite imagery. *The Cryosphere* 15, 5115–5132. issn: 1994-0424 (Nov. 2021)

Fair, Z., Flanner, M., Brunt, K. M., Fricker, H. A. & Gardner, A. Using ICESat-2 and Operation IceBridge altimetry for supraglacial lake depth retrievals. *The Cryosphere* 14, 4253–4263. issn: 1994-0424 (Nov. 2020).

Fricker, H. A. et al. ICESat-2 Meltwater Depth Estimates: Application to Surface Melt on Amery Ice Shelf, East Antarctica. *Geophysical Research Letters* 48. issn: 19448007 (Apr. 2021).

Hou Y, Liu Z, Zhang T, Li Y. C-UNet: Complement UNet for Remote Sensing Road Extraction. *Sensors*. 2021; 21(6):2153. <https://doi.org/10.3390/s21062153>

Jiang D, Li X, Zhang K, Marinsek S, Hong W, Wu Y. Automatic Supraglacial Lake Extraction in Greenland Using Sentinel-1 SAR Images and Attention-Based U-Net. *Remote Sensing*. 2022; 14(19):4998. <https://doi.org/10.3390/rs14194998>



Parrish, C. E. et al. Validation of ICESat-2 ATLAS bathymetry and analysis of ATLAS's bathymetric mapping performance. *Remote Sensing* 11. issn: 20724292 (2019)

Ronneberger, O., Fischer, P., & Brox, T. (2015). U-Net: Convolutional Networks for Biomedical Image Segmentation. *ArXiv, abs/1505.04597*

Yang, K. & Smith, L. C. (2013). Supraglacial Streams on the Greenland Ice Sheet Delineated From Combined Spectral–Shape Information in High-Resolution Satellite Imagery. *IEEE Geoscience and Remote Sensing Letters* 10, 801–805

Yang, Kang (2019): Supraglacial river and lake analysis. figshare. Software. <https://doi.org/10.6084/m9.figshare.9758051.v1>

Cong, Y., Khanna, S., Meng, C., Liu, P., Rozi, E., He, Y., Burke, M., Lobell, D., & Ermon, S. (2022). SatMAE: Pre-training Transformers for Temporal and Multi-Spectral Satellite Imagery. *ArXiv, abs/2207.08051*.

Mañas, O., Lacoste, A., Giró-i-Nieto, X., Vázquez, D., & López, P.R. (2021). Seasonal Contrast: Unsupervised Pre-Training from Uncurated Remote Sensing Data. *2021 IEEE/CVF International Conference on Computer Vision (ICCV)*, 9394-9403.

Jiao L, Huo L, Hu C, Tang P. Refined UNet: UNet-Based Refinement Network for Cloud and Shadow Precise Segmentation. *Remote Sensing*. 2020; 12(12):2001. <https://doi.org/10.3390/rs12122001>

Wang, D., Zhang, J., Du, B., Xia, G., & Tao, D. (2022). An Empirical Study of Remote Sensing Pretraining. *IEEE Transactions on Geoscience and Remote Sensing, PP*, 1-1.

Robinson, A.E., Völgyes, D., Vermeer, M., Fantin, D.S.M., Sørensen, L.S., Kruse, M.A., & Frosch, S. (2023, May 29). Deep learning-based supraglacial lake extent and depth detection on the Greenland Ice Sheet by combining ICESat-2 and Sentinel-2 data. *Global Space Conference on climate change 2023 (GLOC 2023)*, Oslo, Norway. <https://doi.org/10.5281/zenodo.7981531>

Xie, Q., Dai, Z., Hovy, E.H., Luong, M., & Le, Q.V. (2019). Unsupervised Data Augmentation for Consistency Training. *arXiv: Learning*. <https://doi.org/10.48550/arXiv.1904.12848>



8 Calving Front Locations

8.1 Introduction

Calving Front Locations (CFLs) are important parameters of the ice sheet dynamics of outlet glaciers both on Antarctica and Greenland ice sheets. The front location is defined as the sea-ice border line starting from a land-ice-sea border point and ending in a similar point. Despite this simple definition, the automatic extraction of CFLs from remotely sensed optical satellite imagery is very difficult.

The CFL product is currently not in production.

8.2 Review of scientific background

The detection of CFL is inherently a line prediction problem. Three major classes of algorithms can be found in the literature. The first one is directly predicting a connected line segment. The most notable variant is the active contour segmentation models (Chan & Vese 2001). A major benefit of such models is that connectivity is guaranteed by design, and curve smoothness can be controlled through a smoothness parameter. However, this method is known to be sensitive to initialization, and requires careful feature engineering to design energy functional for the energy function.

The second method is finding local features, e.g., edges, and by extracting such features a local probability could be determined (e.g., Beucher & Lantu ej 1979), with the final prediction achieved via thresholding and optional postprocessing. Due to the large variations in texture, these image generic segmentation approaches have not been attempted for CFL detection.

Mohajerani et al. (2019) proposed a third approach which relies on deep learning-based segmentation utilizing a modified U-Net architecture (Ronneberger et al. 2015). In this approach, firstly a segmentation map is created using a deep learning segmentation network, and secondly the front location is extracted as the border of two classes. Since Mohajerani et al. 2019, three major data sources have been explored for CFL extraction: digital elevation models (DEM) (Dong et al. 2020), synthetic aperture radar (SAR) (Zhang et al. 2019, Baumhoer et al. 2020, Davari et al. 2021) and optical imagery (Mohajerani et al. 2019., Cheng et al. 2019). COLD-ML, ESA-funded precursor of the current work, also used Sentinel-2 based optical imagery and segmented the images into ice and non-ice classes.

Previously published literature used a similar U-Net-like segmentation network with limited field of view. Mohajerani downscaled the image before processing. Unfortunately, this could both compromise the texture detection, as texture might get lost during scaling, and limit the resolution of the final product. Cheng et al. used full resolution imagery, but with limited receptive field. This might pose a problem, for instance textureless regions of an ice sheet and refrozen sea might look similar, and a larger context would be required to identify the difference between the two regions. Zhang and Baumhofer used enlarged receptive fields, 3-4 times increasing the linear sizes.

Cheng et al. introduced longest path-based line branching elimination, describing data augmentation steps in detail as a technique fighting against overfit in CFL detection. They also introduced overlapping window-based inference to improve segmentation map quality.

As a final remark, it is important to highlight that many of the methods described above relied on masking out land regions. While this is a simple and effective solution, it requires an accurate land mask which might not be always available.

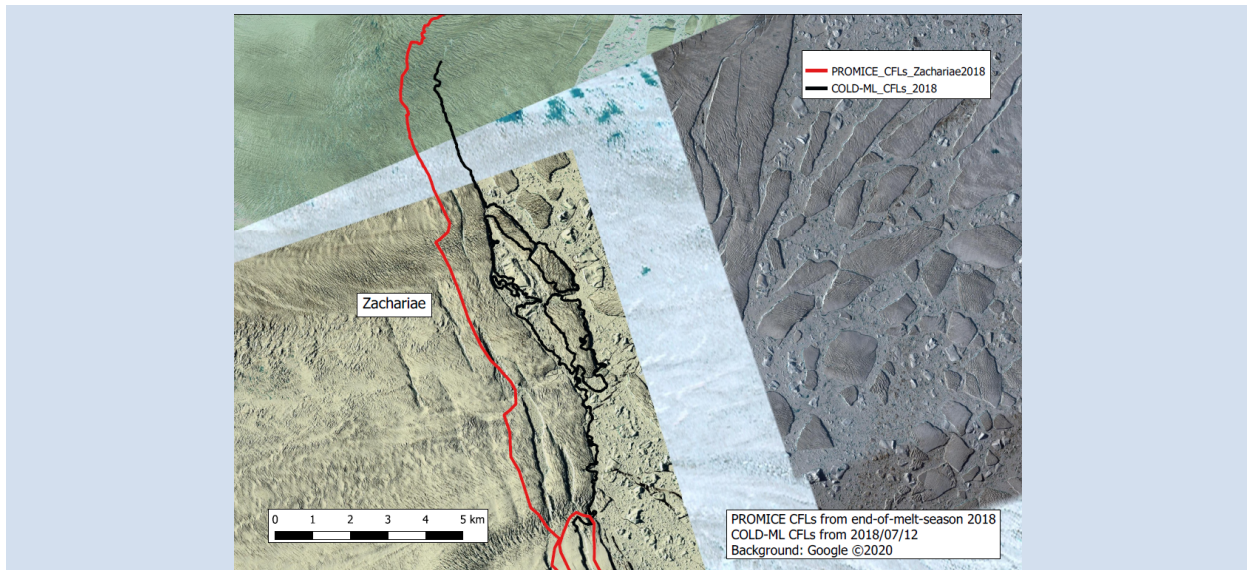


Figure 8.1: Postprocessing of front-locations is required for removing meandering structures (Source: ST-ESA-COLD-ML-D1D2D3-001, Fig 5.7).

8.3 Algorithms

The main limitations identified at the end of the COLD-ML project were:

- The usage of only two classes to predict glacier pixels and ocean pixels. This has led to the need of chopping predictions with a land mask to avoid false front prediction inside land area.
- Another limitation was the size of the receptive field of the architecture which had approximately 1.3km x 1.3 window size. This strongly limits the detection of larger structures, for instance several km long sea ice, major icebergs, or texture less glacier regions.
- Very limited post-processing, with large space for improvement in the handling of the following:
 - Small patches of classes, speckle patterns, etc.
 - Smoothing of the vectorized prediction to remove meandering structures (Figure 8.1).
- The model was able to process only cloud-free images.

To overcome these challenges and improve the prototype developed during the COLD-ML project an algorithm with the following characteristics has been implemented:

Segmentation model

1. The segmentation model for Sentinel-2 10m resolution imagery uses 4 classes. The classes are land, sea and sea-ice, land ice, and clouds and others. The segmentation network is designed specifically for having a large (>10km) receptive.
2. Artificial clouds are incorporated into the augmentation transformations. Cloud template generation algorithm is used to generate alpha masks from cloud-free and cloud covered images from the same scene. The alpha mask extraction is built on Smith & Blinn 1996 alpha matte extraction algorithm. This step is only used for model training data generation, and it is not used for front localization.

Post-processing

1. Speckle noise removal algorithm using connected components labelling algorithm with thresholding.

2. Vectorization of the front location from the segmentation raster.
3. Smoothing of the front location prediction to eliminate meandering predictions.

In summary, the presented algorithm design removes the need of manual processing of images or dependency on external data, e.g., land masks, and produces CFLs directly from Sentinel-2 L1C imagery.

8.4 Input data and algorithm output

The input of the CFLs detection algorithm is the 10m bands of Sentinel-2 L1C imagery. The algorithm performs best with cloud free images, but partial cloud coverage might be acceptable.

The main segmentation algorithm is only tuneable with retraining, but the noise filtering step and the front location smoothing are adjustable if required.

The generated output is a georeferenced shape file containing the CFLs.

8.5 Processing

The schematic workflow of the processing is shown in Figure 8.2.

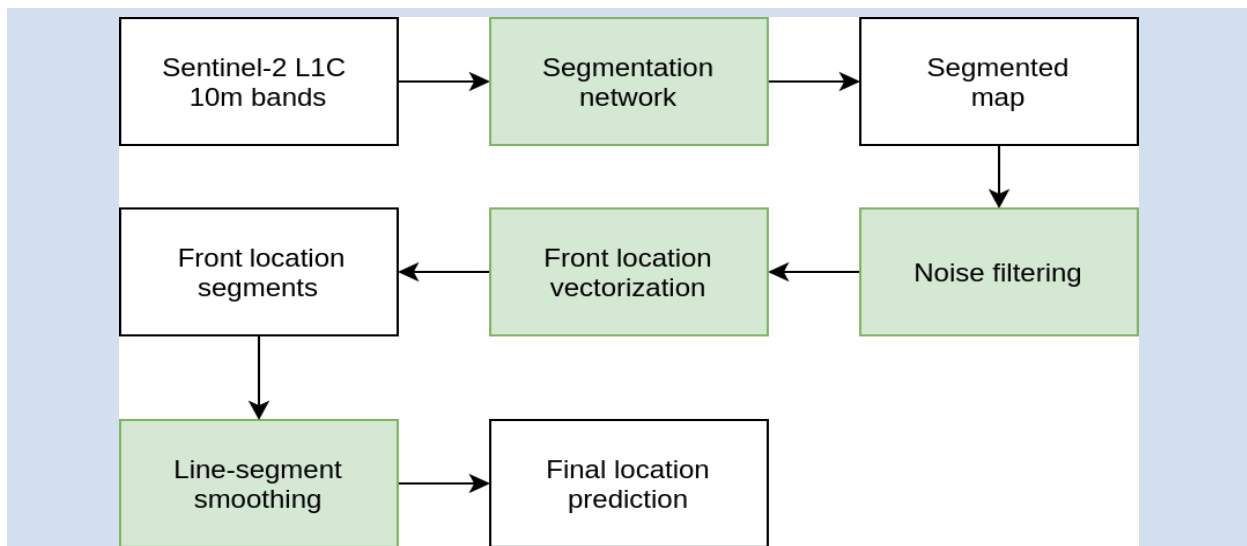


Figure 8.2: Workflow of the CFL detection algorithm. Green boxes represent processing steps, white boxes represent data

8.6 Capabilities and limitations

Optical identification of the CFL primarily depends on the visibility of the front. The major segmentation challenges are snow over land, which makes the land detection less reliable, sea ice in front of the front, and lack of texture on glacier surface. These challenges are seasonal: severe during the winter, least present at the end of the summer season. Icebergs, which can be misidentified as land ice, are more common in the summer. Another limitation is the presence of clouds. Indeed, the cloud “texture” can either render the front location invisible, making it impossible to detect the front location, or look like surface textures which makes the segmentation problem difficult.



8.7 References

- Baumhoer, Celia A., Andreas J. Dietz, C. Kneisel, and C. Kuenzer (2019). "Automated Extraction of Antarctic Glacier and Ice Shelf Fronts from Sentinel-1 Imagery Using Deep Learning" *Remote Sensing* 11, no. 21: 2529. <https://doi.org/10.3390/rs11212529>
- Beucher, S., Lantuéj, C. (1979). Use of watersheds in contour detection. In *Proceedings of the International Workshop on Image Processing*. CCETT.
- Chan, T. F., & Vese, L. A. (2001). Active contours without edges. *IEEE Transactions on image processing*, 10(2), 266-277. <https://doi.org/10.1109/83.902291>
- Cheng, D., Hayes, W., Larour, E., Mohajerani, Y., Wood, M., Velicogna, I., & Rignot, E. (2020). "Calving front machine (CALFIN): Glacial termini dataset and automated deep learning extraction method for Greenland 1972–2019". *The Cryosphere Discussions*, 2020, 1-17. <https://doi.org/10.5194/tc-2020-231>
- Davari, A., Baller, C., Seehaus, T., Braun, M., Maier, A., & Christlein, V. (2021). Pixel-wise Distance Regression for Glacier Calving Front Detection and Segmentation. *arXiv preprint arXiv:2103.05715*.
- Dong, Y., Krieger, L., Floricioiu, D., and Zhao, J. (2020): "Glacier calving front extraction from TanDEM-X DEM products of the Antarctic Peninsula", *EGU General Assembly 2020*, Online, 4–8 May 2020, EGU2020-20137, <https://doi.org/10.5194/egusphere-egu2020-20137>,
- Mohajerani, Yara, Michael Wood, Isabella Velicogna, and Eric Rignot. (2019). "Detection of Glacier Calving Margins with Convolutional Neural Networks: A Case Study" *Remote Sensing* 11, no. 1: 74. <https://doi.org/10.3390/rs11010074>
- Ronneberger, O., Fischer, P., & Brox, T. (2015). U-net: Convolutional networks for biomedical image segmentation. In *International Conference on Medical image computing and computer-assisted intervention* (pp. 234-241). Springer, Cham. https://doi.org/10.1007/978-3-319-24574-4_28
- Smith, A. R., & Blinn, J. F. (1996). "Blue screen matting". In *Proceedings of the 23rd annual conference on Computer graphics and interactive techniques* (pp. 259-268). <https://doi.org/10.1145/237170.237263>
- Zhang, E., Liu, L., & Huang, L. (2019). "Automatically delineating the calving front of Jakobshavn Isbræ from multitemporal TerraSAR-X images: a deep learning approach". *The Cryosphere*, 13(6), 1729-1741. <https://doi.org/10.5194/tc-2019-14>



End of document